Journal of Translational Medicine

RESEARCH

Open Access

Single-cell profiling of tumor lineage plasticity and the immune microenvironment in transformed small cell lung cancer

Jie Huang[1,6†], Zhenhua Zhang[2†], Guodi Cai[2†], Weiye Huang[3], Yu-Qing Chen[1], Jian Zhang[4], Lei Yang[1], Qing Zhou[1], Jin-Ji Yang[1*] and Junjian Wang[2,5*]

Abstract

Background The transformation of non-small cell lung cancer (NSCLC) into small cell lung cancer (SCLC) is a recognized treatment resistance mechanism, most often arising from EGFR-mutant lung adenocarcinoma (LUAD). However, the underlying mechanisms of transformation remain poorly understood.

Methods Single-cell RNA sequencing was employed to analyze the tumor cell heterogeneity and to map the intratumoral immune cell landscape of 73,195 cells from five LUAD, three transformed small cell lung cancer (T-SCLC) and four SCLC patients. Multiplex immunofluorescence (mIF) staining and in vitro studies were further conducted to validate the stem-like feature of a malignant cell cluster and the enrichment and the function of interferon-stimulated gene-positive (ISG^+) lymphocytes in transformation.

Results Although increased intratumoral heterogeneity was observed upon SCLC transformation, a stem-like malignant cell subpopulation was identified to recur across subtypes and groups as the pioneering force of lineage plasticity for SCLC transformation. Further mIF staining and transcription factor analysis validated the stem-like feature. Additionally, tumor immune microenvironment (TIME) analysis revealed that ISG^+ T cells and B cells were enriched in T-SCLC. Further cell co-culture analyses disclosed that ISG^+ lymphocytes promoted neuroendocrine differentiation in LUAD cells via type I interferons (IFN-Is). Deciphering cell-cell interactions revealed that the stem-like malignant cells might activate and attract ISG^+ T cells. Finally, we developed an ISG-associated gene signature that significantly correlates with poor prognosis in LUAD.

Conclusion Our findings provide a comprehensive understanding of the lineage plasticity and the immune landscape in T-SCLC, highlighting the crucial role of the stem-like cell cluster and ISG^+ lymphocytes in LUAD-to-SCLC transformation.

Keywords Transformed SCLC, Lineage plasticity, Stemness, MX1, IFN

†Jie Huang, Zhenhua Zhang and Guodi Cai contributed equally to this work.

*Correspondence:
Jin-Ji Yang
yangjinji@gdph.org.cn
Junjian Wang
wangjj87@mail.sysu.edu.cn

Full list of author information is available at the end of the article

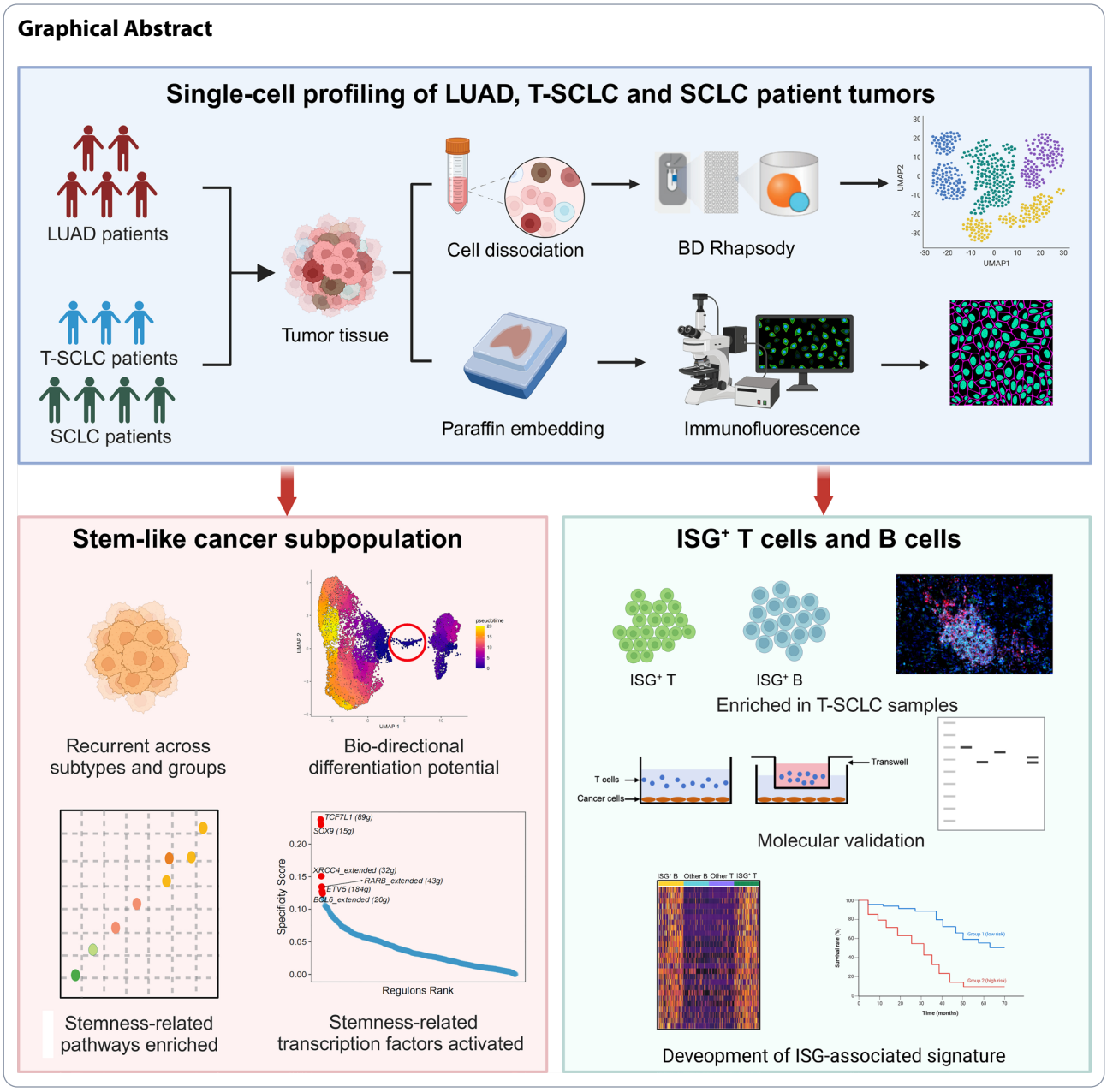

Introduction

Transformed small cell lung cancer SCLC (T-SCLC), as a new phenotype of small cell lung cancer (SCLC), arises from non-small cell lung cancer (NSCLC) under the selective pressure of targeted therapy, chemotherapy, immunotherapy, or even spontaneously without treatment [1]. As an important mechanism of resistance to epidermal growth factor receptor tyrosine kinase inhibitors (EGFR-TKIs), SCLC transformation is the most extensively documented in EGFR-mutant lung cancer patients [2–4]. In these cases, T-SCLC retains the *EGFR* mutations originally present in the NSCLC stage while adopting the aggressive behaviors as SCLC. The median overall survival (OS) from the time of SCLC transformation was only 10.9 months, even worse than *de novo* SCLC [4, 5]. Until now there is no standard treatment established for T-SCLC. Hence, a comprehensive molecular understanding of T-SCLC holds the promise of developing innovative and effective treatment strategies.

While T-SCLC was initially regarded as a homogeneous entity, the significant heterogeneity is increasingly recognized for this malignancy, as recent analyses revealed distinct transcriptomic subtypes of T-SCLC as *de novo* SCLC based on the relative expression of achaete-scute homologue 1 (*ASCL1*), neurogenic differentiation factor 1 (*NEUROD1*), POU class 2 homeobox 3 (*POU2F3*) and

Yes 1 associated transcriptional regulator (*YAP1*) [6, 7]. Lineage plasticity is well recognized as a driving force for cell-state transitions, ultimately leading to SCLC transformation [8]. This raises new questions, such as whether there is plasticity between subtypes and whether a small subpopulation with stem-like, high-plasticity features recurs across different subtypes. However, most of the current data relies on bulk DNA and RNA sequencing, which is only able to estimate the average clonal genotype of a tumor with low representation, making it difficult to distinguish malignant cells or dissect the intratumoral heterogeneity.

The tumor immune microenvironment (TIME) plays a critical role in carcinogenesis, progression and drug resistance. Cancer cells can modify the surrounding TIME, which in turn regulates cancer cell behavior. Previous studies reported that T-SCLC exhibits a progressive suppression of anti-tumor immune response pathways compared with pre-transformation tissue, similar to the immune features of SCLC as a "cold" tumor [7]. We also characterized the decreased levels of CD8 T cells and NK cells, alongside increased infiltration of M2 macrophages during the process of SCLC transformation [9]. Despite these findings, the unique scenario of TIME in T-SCLC remains largely undefined. The application of single-cell RNA sequencing (scRNA-seq) technology provides valuable insight into the interactions between distinct cell types in the TIME, potentially elucidating how the TIME characteristics contribute to SCLC transformation.

Here, we applied scRNA-seq on fresh tumor tissues from T-SCLC, as well as comparative lung adenocarcinoma (LUAD) and *de novo* SCLC, to characterize the tumor cells and TIME landscape of T-SCLC. Our study identify a previously unidentified tumor cell cluster with stem-like characteristics as the pioneering force of lineage plasticity. Moreover, TIME analysis determined the abundance and the crucial role of interferon-stimulated genes-positive (ISG^+) lymphocytes in SCLC transformation. Further cell-cell interaction revealed the crosstalk between ISG^+ T cells and the stem-like malignant cells. Together, our study provides the first comprehensive and in-depth characterization of the cellular and molecular features of T-SCLC.

Methods

Patient selection

The study was approved by the Research Ethics Committee of Guangdong Provincial People's Hospital (No. GDREC2019304H(R1)). All patients with T-SCLC and SCLC provided written informed consent for participation. Tumor tissues were freshly obtained from patients undergoing lymph node biopsy at the hospital. A total of twelve samples were collected from twelve patients (Table S1). Among those, four samples were from treatment-naïve SCLC patients, three were from T-SCLC patients who had transformed from EGFR-mutant NSCLC following treatments, and the remaining five samples were from LUAD patients, which had been reported in a previous study [10]. After resection and biopsy, tumor-tissue samples were immediately transferred for tissue preparation and subjected to single-cell isolation.

Single-cell dissociation

Tissues were placed in MACS Tissue Storage Solution (Miltenyi Biotec) until processing. Tissue samples were processed as described in previous study [11].

Single-cell RNA sequencing and analysis

Single-cell RNA-seq experiment was performed by NovelBio Bio-Pharm Technology Co., Ltd. The detailed method of scRNA-seq pipeline and scRNA analysis were the same as previous described [11]. The public single-cell gene expression profiles of LUAD samples were downloaded from the Gene Expression Omnibus (GSE131907). We merged and integrated this public dataset with our data following the Scanpy workflow [12]. Firstly, we applied the log1pCP10K normalization on the raw counts and selected highly variable genes. Next, we regressed out the effects of the total count per cell and the percentage of mitochondrial gene count. Then, the first 50 principal components were calculated and sample-level batch effects were removed using the Harmony package [13]. Utilizing a graph-based cluster method, we finally acquired unsupervised cell clusters based on the top 10 principal components and annotated the clusters referring to the expression patterns of literature-derived marker genes.

CNV estimation

T cells and fibroblasts were used as reference cell types to identify somatic copy number variations (CNVs) using the infercnv R package (version 0.8.2). Each cell was scored based on the extent of its CNV signal, which was defined as the mean of the squared CNV values across the genome. Putative malignant cells were defined as those with a CNV signal greater than 0.05 and a CNV correlation greater than 0.5.

Differentially abundant subpopulation analysis

To detect differentially abundant subpopulations among the three groups and within each patient, we used the DA-seq algorithm [14]. Significant group-specific cells were identified, corrected for FDR, and visualized using contour plots.

Pseudo-time analysis

Monocle 3 alpha (http://cole-trapnell-lab.github.io/monocle-release/monocle3/) [15] was applied as an independent tool to construct single-cell trajectories. The function learn graph was run with default parameters on on the top 1,000 DEGs, identified using the differentialGeneTest function (expressed in at least 300 cells with an FDR < 0.05).

Differential gene expression analysis

To identify DEGs, the FindMarkers function in the Seurat package was used, employing the Wilcox rank-sum algorithm with the following criteria: lnFC > 0.25, $p < 0.05$, and min.pct > 0.1. The p-value calculated by the wilcox rank-sum test was adjusted using the FDR.

Gene enrichment analysis

Curated gene sets, including Hallmark, KEGG and Reactome gene sets ($n = 910$), were downloaded from the Molecular Signature Database (MSigDB, http://software.broadinstitute.org/gsea/msigdb/index.jsp). Single-sample Gene Set Variation Analysis (ssGSVA) was applied to the scRNA-seq data, and pathway scores were calculated for each cell using the gsva function in the GSVA software package [16]. Pathway enrichment analysis was conducting using the limma R software package, and significantly enriched signaling pathways were identified with an FDR Q value < 0.01.

Multiplex immunofluorescence (mIF) assay and analysis

For multiplex immunofluorescence staining, the following markers were used: CD3 (Abcam, ab16669, 1:1000), visualized with Cy3-Tyramide (1:500); CD20 (Proteintech, 60271-1-Ig, 1:100), visualized with Cy5-Tyramide (1:500); MX1 (Sigma-Aldrich, MABF938, 1:200) and KRT5 (Servicebio, Cat#GB111246, 1:1000), visualized with if488-Tyramide (1:500); SOX9 (Cell Signaling technology, Cat#82630, 1:200), visualized with if555-Tyramide (1:500); ALDH1A1 (Santa Cruz, Cat#sc-374149, 1:100), visualized with if647-Tyramide (1:500) and nuclei were stained with DAPI (1:1000). The slides were scanned using the Pannoramic MIDI (3DHISTECH). Quantification of positive area (μm²), tissue area (μm²), and co-localization positive area (μm²) was performed using the Area Quantification FL v2.1 module in Halo v3.0.311.314 software (Indica labs).

Epithelial cluster 5 (epi 5)-associated gene module construction and scoring

We constructed epi5-associated gene module based on the top 30 genes ranked by log2 fold change in the epi5 cells. The module scores were calculated across mouse samples at different time points during the LUAD-SCLC transition using the UCell R package v.2.0.1 based on the Mann-Whitney U statistic [17]. Briefly, epi5-associated gene list was passed to the ScoreSignatures_UCell function. The resulting cell-wise scores were added to the Seurat object using the AddMetadata Seurat function.

Cell culture

NCI-H1975, HCC827 and HEK-293T cell lines were purchased from American Type Culture Collection (ATCC). NCI-H1975 and HCC827 cells were cultured in RPMI1640 medium, while HEK-293T cells were cultured in DMEM medium. All culture media were supplemented with 10% fetal bovine serum (FBS, Gibco) and 1× penicillin/streptomycin (Gibco). Cells were maintained at 37 °C in a humidified incubator with 5% CO_2.

Culturing of human primary T and B cells, and co-culture

Primary human $CD3^+$ T and $CD19^+$ B cells were purchased from Oricells® (Shanghai AoNeng Biotechnology Co., Ltd.). Collection protocols and donor informed consent were approved by an Institutional Review Board (IRB) at Oricells®. For human $CD3^+$ T cells culture, viable T cells were seeded in fresh RPMI1640 medium supplemented with 10% FBS and 10 ng/mL recombinant human IL-2 (PeproTech) at a density of 1×10^6 cells/mL. To activate T cells, 25 μL/mL of ImmunoCult™ Human CD3/CD28/CD2 T Cell Activator (STEMCELL) was added to the cell suspension. After 3 days of activation, activated T cells were used for gene editing. For human $CD19^+$ B cells culture, viable B cells were seeded in fresh RPMI1640 medium supplemented with 10% FBS and 1 × 2-Mercaptoethanol (Gibco) at a density of 2.5×10^6 cells/mL. To activate the B cells, 10ug/mL of lipopolysaccharides (LPS, Beyotime) was added to the cell suspension. After 2 days of activation, activated B cells were used for gene editing. For tumor-T or tumor-B cells co-culture, NSCLC cells (5×10^5) were seeded in 6-well plates 1 day prior to the addition of an equal number of T or B cells. After 24 h of co-culture, the supernatant containing T or B cells was discarded, and tumor cells were washed twice with phosphate-buffered saline (PBS) before being harvested for protein expression analysis.

MX1 overexpression lentivirus production

For MX1 overexpression, human MX1 cDNA in pLX304 (DNASU) was amplified, and cloned into a modified pLX304 vector with a V5 tag at the N terminus of the receptor. Lentiviral particles were produced in HEK-293T cells after co-transfection of the above lentivirus vectors, psPAX2 and pMD2.G in 10-cm dishes, following the protocol described in our previous study [18, 19]. Activated T and B cells were plated at 2×10^6 cells per well in 6-well plates. A total of 1 mL of virus-containing supernatant with 10 ng of polybrene was added to the cells. After 16 h, the medium was replaced with regular medium, and

the cells were cultured for another 48 h. Then the supernatant was collected by centrifugation at 300 g for 10 min and stored as conditioned medium, while the cells were harvested for protein expression analysis and co-culture experiments.

Type I interferon treatment

Human NSCLC cells were treated with various concentrations of recombinant human IFN-α 2b, IFN-β and IFN-ω (Genscript). Cells were harvested for protein expression analysis 24 h after treatment.

Western blotting

Western blotting was performed as described in previous work [18]. Cell lysates were analyzed by immunoblotting with antibodies specifically targeting MX1 and the indicated proteins. The primary antibodies used in this study were as follows: MX1 (1:1000; Sigma-Aldrich; Cat# MABF938); Chromogranin A (1:1000; Abcam; Cat#ab15160); Synaptophysin (1:1000; Zenbio; Cat#R25834); NSE (1:1000; Abcam; Cat#ab53025); GAPDH (1:1000; Cell Signaling technology; Cat#2118).

Identification of the most activated TFs in ISG$^+$ T and B cells

To identify TFs activated in MX1$^+$ T and B cells, we first applied the "fitGAM" function of tradeSeq-1.4.0 R package [20] to identify the most upregulated genes in ISG$^+$ T and B cells according to single-cell RNA-seq data. Based on these results, we then utilized the "findMotifsGenome.pl" function in Homer-4.11 to identify the top 5 most activated TFs that potentially bind to the upregulated genes. Finally, for visualization, we ranked these TFs by significance based on *p*-values.

Cell communication analysis

Cell-cell communication analysis was performed using CellChat-1.1.2 of the R package [21]. First, we first created a CellChat object with the "createCellChat" function, based on the RNA expression matrix and cell information. Ligand–receptor interaction databases, including "Secreted Signaling", "ECM-Receptor", "Cell–Cell Contact", were further used for downstream analyses. We calculated the communication probability by the "computeCommunProb" function. To identify global communication patterns, the "selectK" function was applied to determine the number of patterns for both incoming and outgoing communication, with nPatterns = 6. To analyze the specified pathways, we utilized "plotGeneExpression", "netVisual_heatmap", "netVisual_chord_cell" and "netVisual_individual" functions to visualize the corresponding results.

Construction and validation of the MX1-specific gene signature

To generate a clinically applicable gene expression signature, we performed multistep analysis. First, we compared the gene expression profiles between MX1$^+$ T and B cells and the other T and B cells, identifing DEGs. The DEG list was then filtered based on the following criteria to select the most significant DEGs: an expression fold change > 1.5 or < – 1.5, an FDR < 0.01, and high expression (normalized UMI count > 1, expressed in at least 50% of cells in either group). In total, 65 significant DEGs met these criteria and were used to constructed the MX1-specific gene signature (Table S2).

The signature was then validated using a publicly available dataset, which was downloaded from UCSC Xena (https://xenabrowser.net/datapages/?cohort=GDC%20TCGA%20Lung%20Adenocarcinoma%20(LUAD)%26removeHub=https%3A%2F%2Fxena.treehouse.gi.ucsc.edu%3A443). First, a sample–gene expression matrix (for the 65 signature genes) was extracted from each normalized bulk RNA-seq dataset. Second, for each sample, a score of 1 or – 1 was assigned to each of the 12 signature genes based on its relative expression (> or ≤ median value). These scores were then summed to create a signature score for each sample. Finally, the samples were categorized into high-activity or low-activity groups based on their corresponding signature scores: scores ≤ median were categorized as low-activity, and scores > median were categorized as high-activity. The Cox proportional hazards model, implemented in the R package "survival", was used to adjust for tumor stage and MSI-status in survival analyses. Kaplan-Meier survival curves were generated using the R function "ggsurvplot".

siRNA transfection

siRNAs targeting interferon alpha and beta receptor subunit 1 (IFNAR1) gene were purchased from Sangon Biotech (Shanghai, China). The siRNA target sequences for IFNAR1 are listed in Table S3. For siRNA knockdown, NSCLC cells were transfected with control or IFNAR1 siRNA using DharmaFECT (Dharmacon, USA) according to the manufacturer's guidelines.

qRT-PCR

Total RNA was isolated from cells in 6-well plates using the TRIeasy® Total RNA Extraction Reagent (YEASEN, Shanghai, China). Following genomic DNA removal, total RNA was reverse transcribed into cDNA. qRT-PCR was amplified and measured on the Bio-Rad CFX96 (Bio-Rad, USA) in the presence of SYBR Green master mix (YEASEN, Shanghai, China). Then, the fluorescence values were collected, and a melting-curve analysis was performed. Primers are listed in in Table S4.

Statistical analysis

All statistical analyses were performed by GraphPad Prism software, version 8. Data are presented as the means ± SD. Statistical comparisons between groups were performed using two-tailed Student's *t*-tests, and a *p*-value of < 0.05 was considered statistically significant.

Results

Single-cell gene expression atlas of T-SCLC, LUAD and SCLC

To characterize the gene expression atlas of T-SCLC tumors at the single-cell level, we prospectively collected seven fresh tumor clinical samples respectively from three T-SCLC patients and four *de novo* SCLC patients. Moreover, publicly available scRNA-seq data from five LUAD patients were analyzed as controls (Fig. 1A). Accordingly, all of the samples were divided into three groups: LUAD, T-SCLC and SCLC, all of which were collected from lymph node metastases. Moreover, both *de novo* SCLC and LUAD patients were treatment-naive prior to biopsy, while T-SCLC patients underwent biopsy after developing resistance to EGFR TKI-targeted therapy. In addition, two of the five samples from the LUAD group harbored *EGFR* mutations, and all samples from T-SCLC patients retained the *EGFR* mutations from their LUAD origin (Table S1).

We analyzed a total of 73,195 single cells after quality control, comprising 24,422 malignant cells and 48,773 nonmalignant cells. All of the cells were classified into the following eight major types according to their canonical markers: epithelial cells (*EPCAM*, *KRT19*, *KRT18*, *INSM1*), proliferative epithelial cells (*TOP2A*, *MKI67*), fibroblast cells (*COL1A1*, *FN1*, *DCN*, *LUM*), endothelial cells (*PECAM1*, *VWF*, *PLVAP*, *CD34*), T cells (*CD2*, *CD3E*, *CD3D*, *NKG7*), plasma cells (*IGHG1*, *MZB1*, *JCHAIN*), B cells (*CD79A*, *MS4A1*, *CD79B*) and myeloid cells (*LYZ*, *CD14*, *CD68*, *CD163*) (Fig. 1B). Top 10 differential gene expression further confirmed the identification of each cell type (Figure S1A).

We conducted comprehensive cell-type annotations for each group and each patient using established markers and computational tools (Fig. 1C). Similar to the observations in previous studies [22, 23], stromal and immune cells from different patients tended to cluster together by cell types, indicating that these cell types exhibit largely conserved expression profiles across patients, despite variations in their relative proportions. However, epithelial cells showed higher heterogeneity and group-specific expression signatures, which may be associated with the histological diversity characteristic of different patient groups. Notably, proliferative epithelial cells were significantly enriched in the SCLC group compared to the T-SCLC and LUAD groups, consistent with the characteristic of rapid proliferation in SCLC (Fig. 1D).

To characterize the TIME remodeling during SCLC transformation, we calculated the fraction of different cell types in the LUAD, T-SCLC and SCLC groups (Fig. 1E). We observed a decreased fraction of T cells in the SCLC group, consistent with previous reports characterizing the 'immune desert' phenotype commonly seen in SCLC. In addition, B cells and plasma cells were predominant in the T-SCLC group, but statistical analysis showed no significant difference ($p>0.05$), likely due to limited sample sizes. Myeloid cells were enriched in the LUAD group, while fibroblast and endothelial cells were almost absent, possibly due to the biopsy type of endobronchial ultrasound-guided transbronchial needle aspiration (EBUS-TBNA), which is less likely to capture stromal components (Figure S1B).

Heterogeneity of T-SCLC malignant cells at single-cell resolution

A total of 24,422 epithelial cells were obtained and almost all of them were distinguished as malignant cells by inferred copy-number variation (CNV) analysis (Figure S2). Consistent with previous studies [23, 24], epithelial biomarkers, such as epithelial cell adhesion molecule (*EPCAM*) and insulinoma-associated protein 1 (*INSM1*), were uniformly expressed at high levels across LUAD and SCLC malignant cells (Figure S3A). All of the malignant cells were classified into six clusters (Fig. 2A). The total malignant cell proportions were similar between the T-SCLC group and the SCLC group, whereas cluster 6 occupied the majority of the epithelium compartment in the LUAD group (Fig. 2B). Most of the cells from the LUAD group were assigned to a single cluster, while the cells from the T-SCLC and SCLC groups spread across multiple clusters, indicating increased intertumoral heterogeneity during the transformation from LUAD to SCLC (Fig. 2B).

Cluster 1 exhibited highly proliferative characteristics, suggested by the significantly high expression levels of cell cycle-related genes such as *TOP2A*, *CENPF* and *MKI67* (Fig. 2C and S3B). Cluster 1 was mainly composed of cells from the SCLC and T-SCLC samples, with minimal presence in the LUAD group (Fig. 2B), in agreement with much fewer proliferative epithelial cells in the LUAD group (Fig. 1D). Cluster 2, which comprised cells mainly from the SCLC and T-SCLC groups, exhibited upregulated expression of neuroendocrine-related genes such as *HES6*, *INSM1*, *SCGN* and *DLL1*, validating the neuroendocrine characteristics of SCLC (Fig. 2C and S3B). *ASCL1*, as a canonical transcription factor for SCLC, was widely expressed across multiple clusters and strongly expressed in Cluster 3, while another lineage transcription factor, *NEUROD1*, was exclusively expressed in Cluster 4 (Fig. 2C). Both of them were previously implicated as key determinants in the

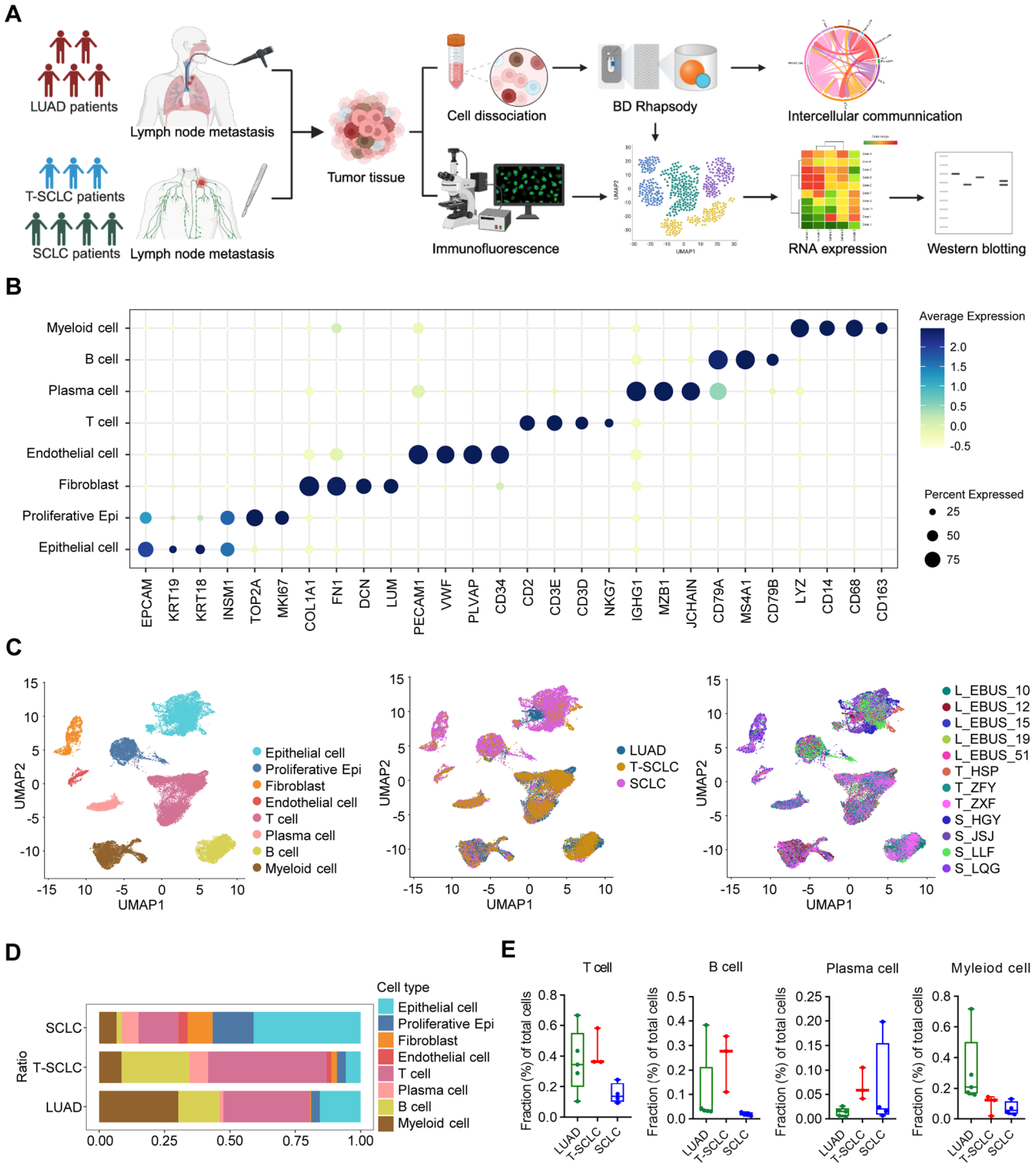

Fig. 1 scRNA-seq profiling of the landscape of T-SCLC. (**A**) Workflow of the sample collection, sequencing, bioinformatic analysis and validation. (**B**) Bubble plot of canonical marker genes for each cell type. (**C**) The uniform manifold approximation and projection (UMAP) plot of all clustered cells, color-coded by cell type, group, and patient. (**D**) Proportions of cell types in each group. (**E**) Boxplot showing the cellular fractions of T, B, plasma and myeloid cells in LUAD ($n=5$), T-SCLC ($n=3$), and SCLC ($n=4$) patients. The center line indicates the median value, the lower and upper hinges represent the 25th and 75th percentiles, respectively, and whiskers denote 1.5× the interquartile range. Each dot represents to one sample

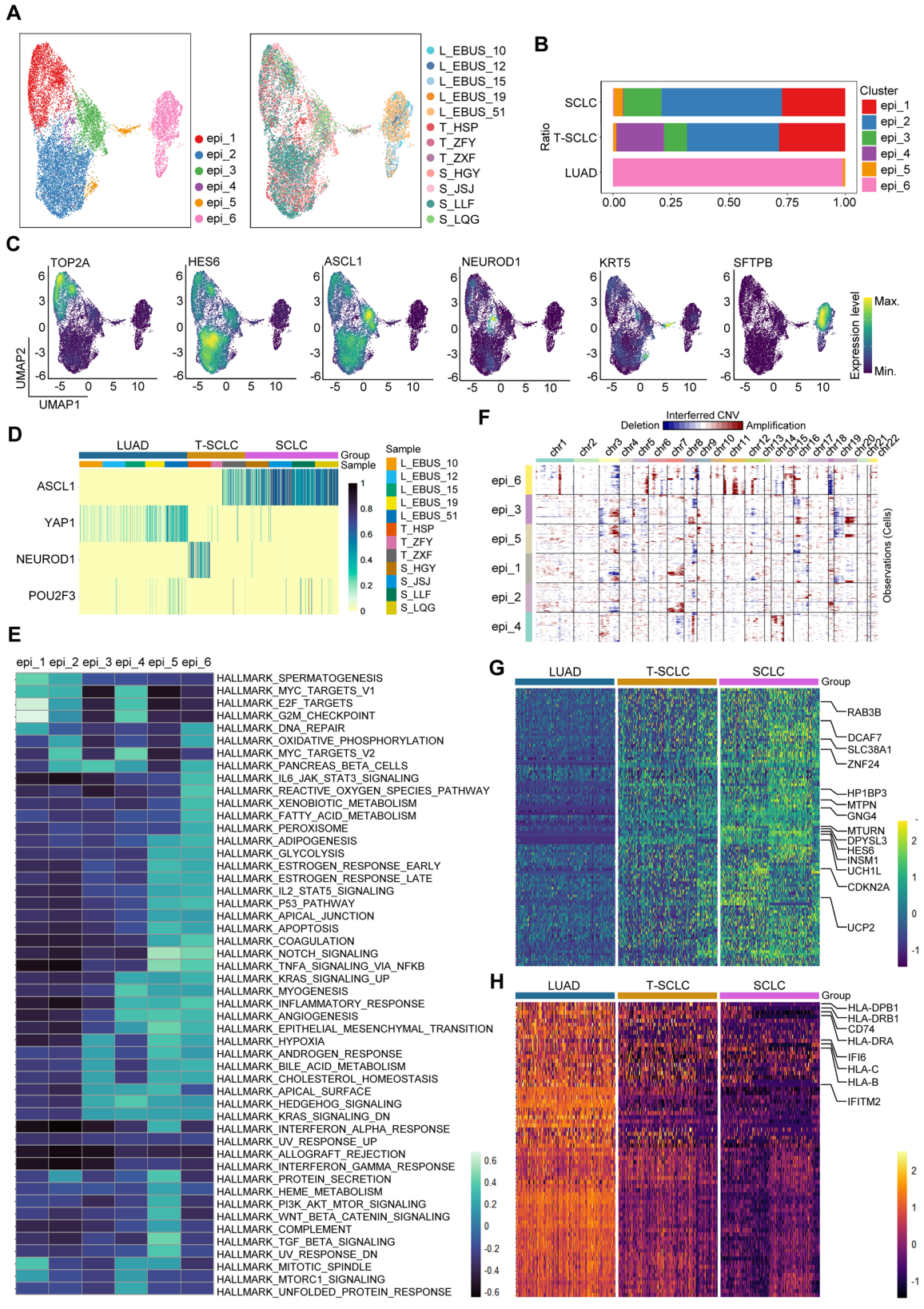

Fig. 2 (See legend on next page.)

(See figure on previous page.)

Fig. 2 Heterogeneity of T-SCLC malignant cells at single-cell resolution. (**A**) UMAP plot of epithelial cells clustered and color coded by cluster and patient. (**B**) The proportion of each cluster across the three groups. (**C**) UMAP plot of canonical marker genes for each cluster. (**D**) Expression of *ASCL1*, *NEUROD1*, *YAP1* and *POU2F3* in epithelial cells from each patient. (**E**) Pathway enrichment analysis using the hallmark gene set collections for each cluster. (**F**) Copy number variation (CNV) inference across chromosomes (columns) with amplification (red) and deletions (blue) based on cluster. (**G**) Heatmap highlighting differentially expressed genes (DEGs) progressively upregulated from LUAD to T-SCLC to SCLC. (**H**) Heatmap highlighting DEGs progressively downregulated from LUAD to T-SCLC to SCLC

developmental maturation of neuroendocrine cells in the lung [25, 26]. Cluster 5, the only cluster recurring across the three groups, showed upregulated expression of the basal cell markers, *KRT5* and *TP63*, suggesting a basal cell origin (Fig. 2C and S3B). Cluster 6, which was specific to the LUAD group, showed obviously high expression of the canonical markers (*SFTPB*, *SFTPA1*, *SFTPA2* and *SLC34A2*) of alveolar type 2 (AT2) cells, suggesting an origin from AT2 cells, which is consistent with previous reports that AT2 cells could develop into LUAD cells [27, 28] (Fig. 2C and S3B).

Based on differential expression of *ASCL1*, *NEUROD1*, *POU2F3* and *YAP1*, *de novo* SCLC can be classified into four molecular subtypes: SCLC-A, SCLC-N, SCLC-P and SCLC-Y [29]. Although T-SCLCs conform to all major subtypes of *de novo* SCLCs based on bulk-RNA sequencing [6], the bulk approach lacks the resolution to reveal cell-to-cell heterogeneity. We next explored whether individual malignant cells could vary according to these classifications (Fig. 2D). Our results revealed that *ASCL1* was highly expressed in almost all tumor cells of four SCLC samples and one T-SCLC sample. These five SCLC-A tumors consisted of a large number of cells uniformly expressing high levels of *ASCL1*, while only a few cells expressed one of the other three transcription regulators (*NEUROD1*, *POU2F3* and *YAP1*). Another tumor from the T-SCLC group mapped to SCLC-N, with most individual cells expressing high levels of *NEUROD1*. Strikingly, malignant cells from the remaining T-SCLC tumor exhibited low levels of *YAP1* and no detectable expression of *ASCL1* or *NEUROD1*, known as the non-neuroendocrine cells, which suggests the existence of potential new subtype dominated by other transcription factors (TFs). As expected, *YAP1* was mainly expressed in tumor cells of LUAD rather than T-SCLC and SCLC. These single-cell results confirmed the diversity of cancer cell states in T-SCLC and indicated that lineage plasticity could activate diverse transcriptional programs during the SCLC transformation process.

To further explore what biological states or processes involved among individual malignant cells, we performed gene set enrichment analysis (GSEA) using the 'Hallmark' gene set collections for those genes with high variability (Fig. 2E). Clusters 1 and 2 were enriched in cell cycle-related pathways, such as E2F targets, G2M checkpoint and Myc targets. In contrast, cluster 6 was enriched in multiple immune response-related pathways, including inflammatory response, IL6-JAK-STAT3 signaling and TNFA-NFκB signaling, which were distinct from those in clusters 1 and 2. Intriguingly, pathways enriched in clusters 3, 4 and 5 are partially identical to those enriched in cluster 6, as well as clusters 1 and 2. Notably, cluster 5 showed marked upregulation of Notch signaling, epithelial mesenchymal transition (EMT) pathway and PI3K-AKT-mTOR signaling, which are known to play crucial roles in lineage plasticity and neuroendocrine transformation [7, 8].

Next, we used the scRNA-seq data to infer CNVs, revealing the intercluster and intergroup heterogeneity. For cluster 6, prominent arm-level insertions were found in chromosomes 1q, 5q, 6p and 10, along with deletions in chromosomes 14q and 18, while CNVs of other clusters exhibited more patient-specific variations, indicating more significantly intertumor heterogeneity (Fig. 2F). The CNV profiles of the three groups further confirmed higher intratumoral heterogeneity in T-SCLC and SCLC compared to LUAD (Figure S3C).

To further explore the transcriptional changes during SCLC transformation, we performed differential gene expression and pathway enrichment analyses of malignant cells from the three groups. Compared to LUAD, T-SCLC showed increased expression of genes related to neuronal development and differentiation (*HES6*, *DPYSL3*, *MTPN*, *UCHL1*, *INSM1*, *ZNF24* and *MTURN*), cell growth (*GNG4*, *CDKN2A* and *DCAF7*), hypoxia (*UCP2* and *HP1BP3*), Neurotransmitter transport (*RAB3B*, *SLC38A1*), which were further upregulated in SCLC (Fig. 2G). Conversely, progressively downregulated expressions were observed in genes associated with antigen-presentation and interferon response (*HLA-DPB1*, *HLA-DRB1*, *HLA-DRA*, *HLA-C* and *HLA-B*) and genes related to cytokine-mediated signaling pathway (*CD74*, *IFI6* and *IFITM2*). These results indicated that T-SCLC occupied an intermediate state, consistent with prior observation [6] (Fig. 2H).

Identification of a stem-like cell cluster as the pioneering force of lineage plasticity in T-SCLC

Pulmonary basal cells are known to serve as multipotent progenitors, capable of lineage plasticity [30]. Therefore, we performed an in-depth analysis of epithelial cluster 5 (epi 5) which exhibited features consistent with basal cell origin. First, we constructed the development trajectory of epithelial cells using Monocle 3, and pseudotime

analysis revealed that epi 5 was positioned at the beginning of the differentiation trajectory, indicating a highly undifferentiated state with strong differentiation potential (Fig. 3A). Further RNA velocity analysis validated the directionality of differentiation from epi 5 to other epithelial clusters (Figure S3D). In addition, a 3D UMAP projection of epithelial cells further showed that epi 5 occupied a central position, acting as a bridge population connecting two distinct lineages: neuroendocrine cells and AT2 cells (Fig. 3B).

Next, to further understand the characteristics of epi 5 cells, we performed gene expression analysis. The results

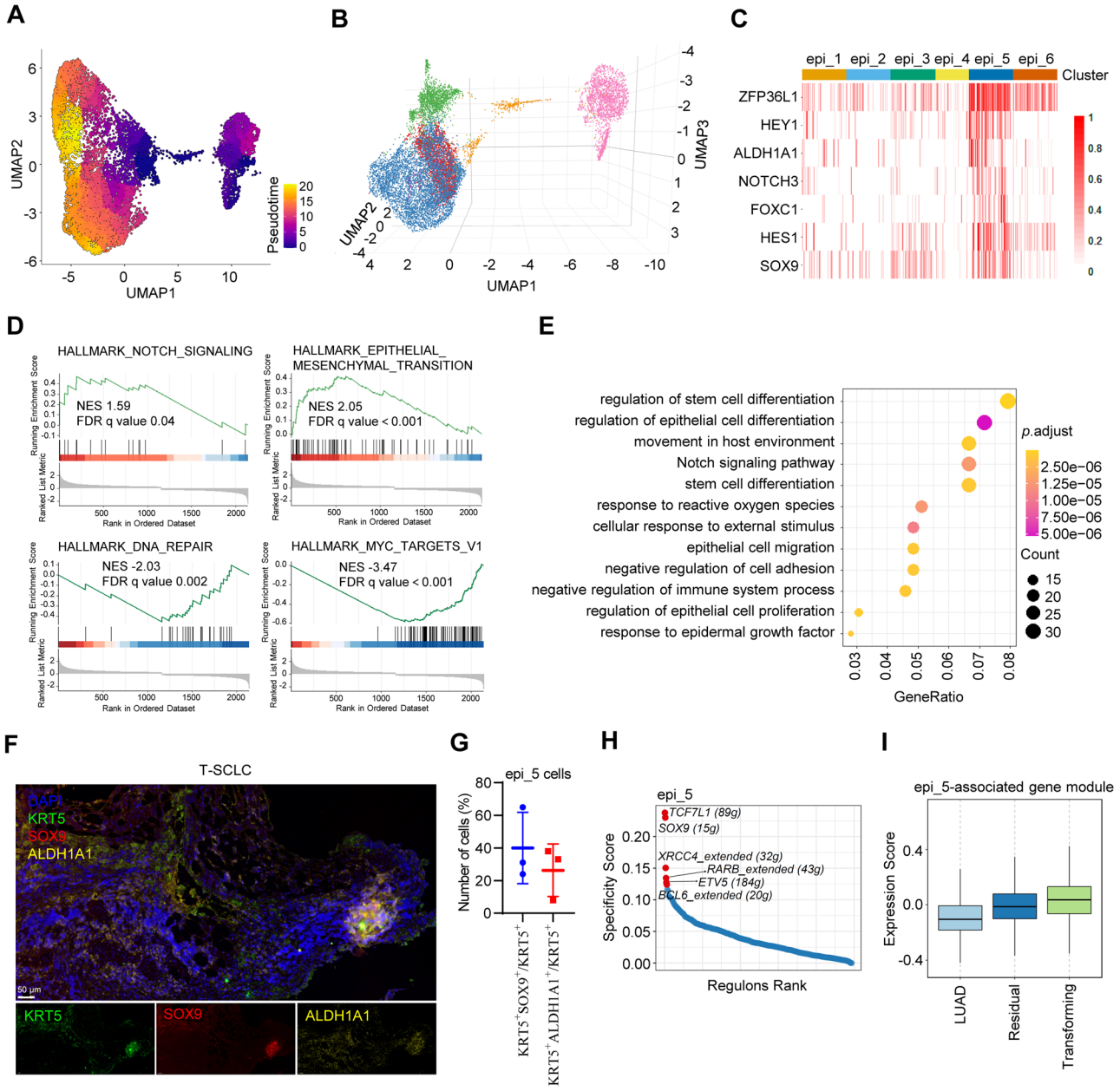

Fig. 3 Identification of a stem-like cell cluster as the pioneering force of lineage plasticity in T-SCLC. (**A**) Monocle 3 pseudotime trajectory analysis revealed different stages of epithelial cell differentiation. The UMAP plot is colored by inferred pseudotime. (**B**) 3D UMAP projection of epithelial cells. (**C**) Expression of stemness-related genes across six epithelial cell clusters. (**D**) The gene set enrichment analysis (GSEA) shows the significantly upregulated and downregulated pathways in epithelial cluster 5 compared to the other five clusters. (**E**) Gene Ontology analysis of differentially enriched biological processes between epithelial cluster 5 and the other clusters. (**F**) Representative images of KRT5, SOX9 and ALDH1A1 in situ multiplex immunofluorescence (mIF) staining in T-SCLC tumor tissues. Scale bars, 50 μm. (**G**) The proportions of $KRT5^+SOX9^+$ cells in $KRT5^+$ cells and $KRT5^+ALDH1A1^+$ cells in $KRT5^+$ cells by mIF co-localization analysis. (**H**) Motif enrichment analysis visualizing critical transcription factors (TFs) activated in epithelial cells from cluster 5. (**I**) The expression scores of epi 5-associated gene module in the primary LUAD, the residual LUAD, and the transforming state

showed that epi 5 exhibited higher expression of stemness-related genes, including *ZFP36L1*, *HES1*, *HEY1*, *SOX9*, *NOTCH3*, *FOXC1* and *ALDH1A1* (Fig. 3C). Consistently, pathway enrichment analysis uncovered pathways related to Notch signaling, stemness differentiation and EMT in epi 5, reflecting the stem-like characteristics of this cluster (Fig. 3D and E). Unexpectedly, MYC-related pathways were obviously downregulated in epi 5. To further validate the stem-like properties of epi5 cells, we performed in situ multiplex immunofluorescence (mIF) staining using antibodies against KRT5, SOX9, and ALDH1A1 (Fig. 3F). Co-localization analysis of mIF data showed the mean proportion of $KRT5^+SOX9^+$ cells in $KRT5^+$ cells was 40%, while that of $KRT5^+ALDH1A1^+$ cells in $KRT5^+$ cells was approximately 26%. These results confirm the presence of epi 5 cells with stem-like characteristics (Fig. 3G).

We then used SCENIC to investigate the TFs activated in epi 5, and the top TFs identified were TCF7L1 and SOX9. TCF7L1 regulates cell differentiation in embryonic stem cells [31], and SOX9, as a stem cell transcriptional regulator, promotes lineage plasticity [32] (Fig. 3H). These findings suggest that epi 5, a stem-like cell cluster, may serve as a pioneering force driving lineage plasticity in SCLC transformation.

In addition, we further validate the existence of the stem-like cell cluster using public scRNA-seq data from a mouse model of histological transformation [27]. First, we constructed an epi 5-associated gene module based on the top 30 genes ranked by log2 fold change in the epi 5 cells. Subsequently, the scores of this gene module were calculated across mouse samples at different time points during the LUAD-SCLC transition. The result showed that the scores of the epi 5-associated gene module increased gradually along the transition from the primary LUAD to the residual LUAD, and then to the transforming state, further reinforcing our findings (Fig. 3I).

ISG^+ T cells were enriched in T-SCLC

The T/natural killer (NK) cell compartment comprised of six major clusters, including naive T cells, $CD4^+$ T cells, $CD8^+$ T cells, proliferating T cells, $CD16^+$ NK cells and $CD56^+$ NK cells according to the differential gene expression (Fig. 4A and B, and S4A). These clusters were widely present across all three groups (Figure S4B). NK cells, known for their innate cytotoxicity, were more abundant in the LUAD group compared to the SCLC and T-SCLC groups. Tumor-infiltrating NK cells in this study exhibited a potent killing capacity, characterized by the preferential expression of killer cell lectin-like receptors (*KLRC1*, *KLRF1* and *KIR2DL4*) and *FCGR3A*, an important receptor for initiating antibody-dependent cellular cytotoxicity [9, 33] (Figure S4C). These results indicate a lower frequency of activated tumor-infiltrating NK cells in SCLC than LUAD, consistent with previous bulk-RNA data [34].

$CD4^+$ T cells and $CD8^+$ T cells were further reclustered into seven and six subgroups, respectively (Fig. 4C and D, S4D and E). Notably, in both $CD4^+$ T and $CD8^+$ T cell subgroups, the proportion of ISG^+ T cells in T-SCLC was significantly higher than in LUAD and SCLC (Fig. 4D and F). Further pseudotemporal trajectory analysis of T cells revealed that $CD4^+$ ISG^+ T cells were in the late stage of $CD4^+$ T cell differentiation, and $CD8^+$ ISG^+ T cells were in the intermediate-to-late differentiation stage of $CD8^+$ T cell differentiation, indicating that these subgroups were well-differentiated and relatively mature (Fig. 4G and H). The marker gene expression and DEG analyses consistently showed high expression of interferon (IFN) activation markers such as *IFI6*, *IFI44*, *ISG15* and *STAT1*, along with interferon stimulated protein (ISP) including *MX1*, *MX2*, the IFIT family and *OAS3*, in both $CD4^+$ ISG^+ and $CD8^+$ ISG^+ T cells, revealing a close association between these subgroups and type I interferon (IFN-I) (Fig. 4I). GSEA further showed prominent enrichment of IFN-I-related pathways, such as IFN-I production, response to IFN-I and RIG-I-like receptor signaling pathways, in ISG^+ T subgroups compared with other subgroups. This indicated that ISG^+ T cells possessed a potent capacity to promote IFN-I production and signaling activation (Fig. 4J). Based on the high similarity between $CD4^+$ ISG^+ T and $CD8^+$ ISG^+ T cells, as indicated by the above results, we next analyzed these two subgroups together, collectively termed as ISG^+ T cells.

To validate the presence of ISG^+ T cells in lung cancer patients, mIF staining was applied in the LUAD, T-SCLC and SCLC tissues with antibodies against CD3, CD20 and MX1 (Fig. 4K). MX1 was selected as it was broadly and significantly expressed in ISG^+ T cells, as suggested by sc-RNA seq data. Unsurprisingly, the mIF results further confirmed the presence of ISG^+ T cells in T-SCLC samples, with a significantly higher abundance compared to LUAD and SCLC samples (Fig. 4L). Moreover, ISG^+ T cells were rarely detected in SCLC samples, consistent with the scRNA-seq results.

Considering the significantly higher proportion of ISG^+ T cells in T-SCLC, we next investigated whether ISG^+ T cells were involved in SCLC transformation. Firstly, we developed a stable MX1-overexpressing subline ($MX1^{OE}$ T cells), representing ISG^+ T cells, by transfecting $CD3^+$ T cells with pLX304-MX1. The corresponding negative control subline (Vector T cells) was generated by transfecting $CD3^+$ T cells with pLX304 empty vector. Western blotting analyses confirmed significantly upregulated MX1 expression in $MX1^{OE}$ T cells as compared with Vector T cells (Fig. 4M). Subsequently, we set up in vitro co-culture experiments using LUAD cell lines (H1975 or HCC827) and $CD3^+$ T cells ($MX1^{OE}$ T

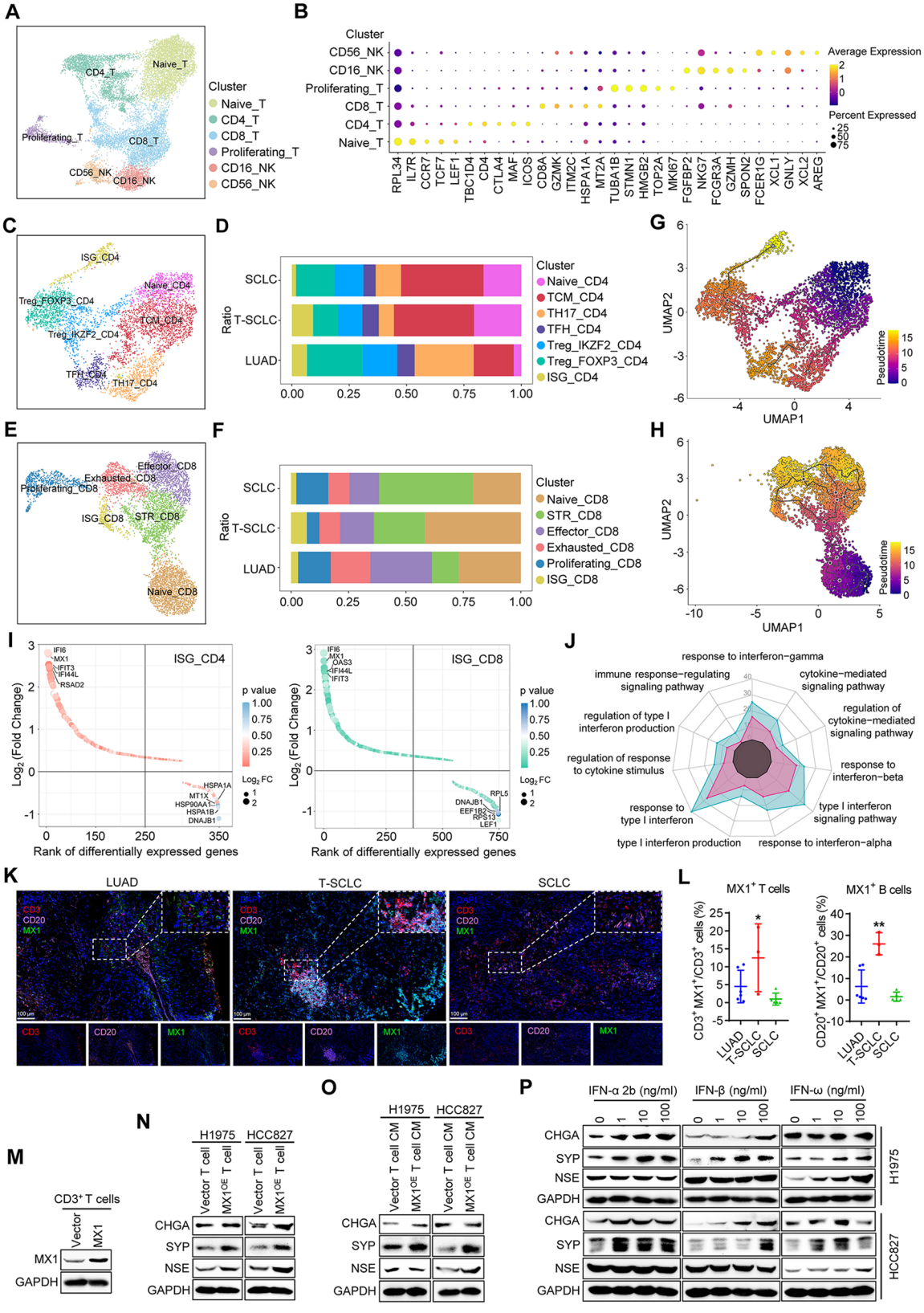

Fig. 4 (See legend on next page.)

(See figure on previous page.)

Fig. 4 Interferon-stimulated genes-positive (ISG^+) T cells were enriched in T-SCLC. (**A**) UMAP plot of total T/NK cells across all samples, color-coded by six clusters. (**B**) Bubble plot shows the top 5 highest expression genes in each cluster. (**C**) UMAP plot of the density of $CD4^+$ T cells color-coded by seven clusters. (**D**) The proportions of the seven clusters of $CD4^+$ T cell clusters across the three groups. (**E**) UMAP plot of the density of $CD8^+$ T cells color-coded by six clusters. (**F**) The proportions of the six clusters of $CD8^+$ T cell clusters across the three groups. (**G**) Monocle 3 pseudotime trajectory analysis revealed different stages of $CD4^+$ T cell differentiation. The UMAP plot is colored by inferred pseudotime. (**H**) Monocle 3 pseudotime trajectory analysis revealed different stages of $CD8^+$ T cell differentiation. (**I**) Significantly upregulated and downregulated genes in the ISG^+ $CD4^+$ and ISG^+ $CD8^+$ T cell clusters. (**J**) Significantly enriched pathways in the ISG^+ $CD4^+$ and ISG^+ $CD8^+$ T cell clusters. (**K**) Representative images of CD3, CD20 and MX1 in situ immunofluorescence staining in the three groups. Scale bars, 100 μm. (**L**) Quantification analysis of immunofluorescence staining in the LUAD group ($n=6$), the T-SCLC group ($n=3$) and the SCLC group ($n=5$). *, $p<0.05$; **, $p<0.01$ compared with the SCLC group, unpaired t-test. (**M**) Western blotting analysis of MX1 protein expression in $CD3^+$ T cells infected with MX1 overexpression ($MX1^{OE}$) or vector lentivirus and incubated for 48 h. (**N**) Western blotting analysis of neuroendocrine markers in H1975 and HCC827 cells after co-cultured with vector or $MX1^{OE}$ T cells for 24 h. (**O**) Western blotting analysis for neuroendocrine markers in H1975 and HCC827 cells after culturing with conditioned medium (CM) from vector T or $MX1^{OE}$ T cells for 24 h. (**P**) Western blotting analysis for neuroendocrine markers in H1975 and HCC827 cells after treatment with different dose of the indicated type I interferon (IFN-α, IFN-β and IFN-ω) for 24 h

or Vector T cells). Compared to Vector T cells, $MX1^{OE}$ T cells markedly promoted the expression of three typical neuroendocrine markers, chromogranin A (CHGA), synaptophysin (SYP) and neuron-specific enolase (NSE), in both H1975 and HCC827 cells, indicating the promotion of neuroendocrine transformation (Fig. 4N). Suspecting that IFN-I cytokines produced by $MX1^+$ T cells were responsible for this effect, we next treated both LUAD cell lines with conditioned medium (CM) collected from the supernatant of $MX1^{OE}$ T or Vector T cells after 48 h culture. Consistently, the expression of neuroendocrine markers was significantly increased in both H1975 and HCC827 cells after treatment with medium conditioned by $MX1^{OE}$ T cells (Fig. 4O), consistent with the the expression of *CHGA/SYP/ENO2* in the scRNAseq data (Figure S4F). Moreover, similar results were also observed in H1975 and HCC827 cells treated with IFN-I (IFN-α, IFN-β or IFN-ω) for 24 h in a dose-dependent manner (Fig. 4P). However, inhibition of the expression of IFNAR1, an important IFN-I receptor gene, using siRNAs significantly impeded the upregulation of CHGA and SYP expression (Figure S4G and H). Cumulatively, these results demonstrated that IFN-I produced by $MX1^+$ T cells may play a crucial role in promoting neuroendocrine differentiation of LUAD cells.

ISG^+ B cells were involved in SCLC transformation

Tumor-infiltrating B cells and plasma cells (TIBs) used to be overlooked and their roles in the immunobiology of solid tumors such as lung cancer remain poorly understood. Here, we detected and characterized TIBs by scRNA-seq. TIBs were divided into two main subtypes: plasma and B cells, with a higher proportion of plasma cells observed in the SCLC group than the T-SCLC and LUAD groups (Fig. 5A). Plasma cells and B cells were further reclustered into 2 and 4 subclusters, respectively, including IgG plasma, IgA plasma, naive B, memory B1, memory B2 and ISG^+ B cells. These subclusters were identified through the top 10 differentially expressed genes (Fig. 5B and S5). As mentioned above, the fractions of B cells among all the cells were markedly enriched in the T-SCLC group compared with the LUAD and SCLC groups (Fig. 1E). In adaptive immunity, naive B cells differentiate into either memory B cells or plasma cells [35]. We next constructed the developmental trajectory of B cells using Monocle 2, and pseudotime analysis revealed various states of B cell differentiation. ISG^+ B cells were widely distributed across the trajectory and were more likely enriched at the early developmental stage (Fig. 5C). The expression levels of IgA, IgG and IgM transcripts further indicated the immature, naive-like status of ISG^+ B cells [35] (Fig. 5D).

Similar to ISG^+ T cells, ISG^+ B cells also showed the upregulated expression of IFN activation markers as well as ISP (Fig. 5E). In addition to the RIG-I-like receptor signaling pathway, the Th1 and Th2 cell differentiation signaling was also markedly enriched in the ISG^+ B cluster, while IL-17 signaling was downregulated (Fig. 5F). This suggests an alternative differentiation pathway of T helper lineage, with a shift from a Th17 cell phenotype towards Th1 or Th2 cells, which is closely related to IFN signaling. The presence of ISG^+ B cells were also validated by mIF staining, revealing a significantly higher abundance of ISG^+ B cells in T-SCLC than LUAD and SCLC (Fig. 4K and L).

Next, we employed motif enrichment analysis to identify critical TFs activated in ISG^+ T and B cells (Fig. 5G and J). The analysis revealed that interferon-regulatory factors (IRFs) and signal transducer and activator of transcription (STAT) proteins were highly upregulated and bound directly to regulatory regions of MX1 in both ISG^+ B and T cells. IRF2 and IRF7 have been shown to be positive regulators of IFN-I production, ISGs expression, and other pro-inflammatory cytokines/chemokines induction. Moreover, IRF7 expression could be induced by IFN-I in ISG^+ T cells, inducing a feedforward loop that further amplified IFN-I expression [36]. IRF9 directly interacts with STAT1:STAT2 heterodimers to comprise interferon-stimulated gene factor 3 (ISGF3) that plays a crucial role in the JAK/STAT pathway and regulates ISG expression in response to IFN-I [37]. In addition, stemness-related TFs NEUROD1 and YY1 were activated in ISG^+ T and B cells, respectively.

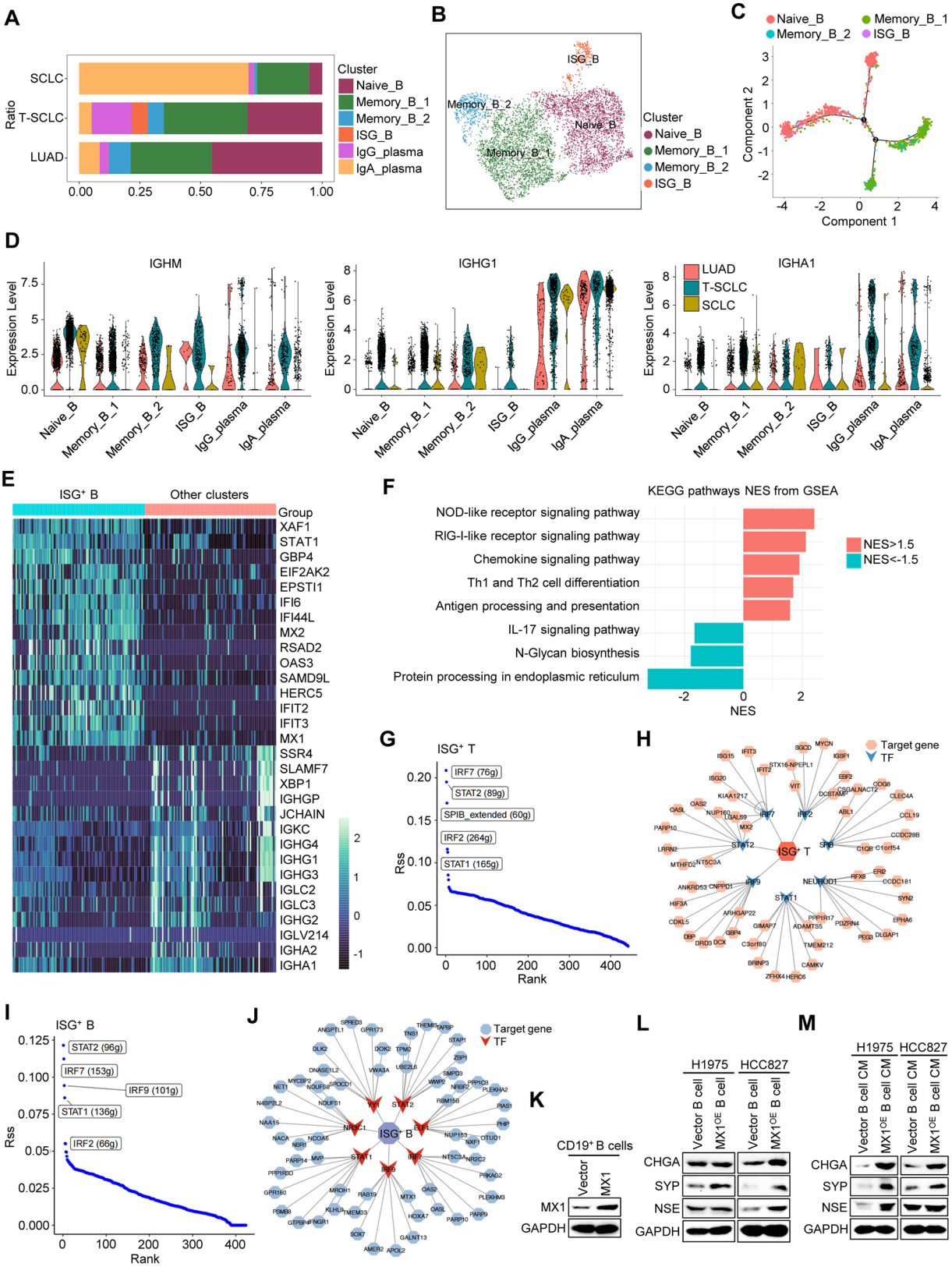

Fig. 5 (See legend on next page.)

(See figure on previous page.)

Fig. 5 ISG$^+$ B cells were involved in SCLC transformation. (**A**) The proportion of each B/plasma cell cluster across the three groups. (**B**) UMAP plot of total B cells divided into four clusters. (**C**) The development trajectory of B cells inferred by Monocle 2. (**D**) Violin plots shows the differences in expression levels of indicated Ig subclass coding genes across six clusters and among the three groups. (**E**) Heatmap of DEGs between the ISG$^+$ B cell clusters and other clusters. (**F**) GSEA shows significantly upregulated and downregulated pathways in the ISG$^+$ B cell cluster compared with other clusters. (**G**, **H**) Visualization of motif enrichment to identify critical TFs activated in ISG$^+$ T cells. (**I**, **J**) Visualization of motif enrichment to identify critical TFs activated in ISG$^+$ B cells. (**K**) Western blotting analysis of MX1 protein expression in CD19$^+$ B cells infected with MX1^{OE} or vector lentivirus and incubated for 48 h. (**L**) Western blotting analysis of the indicated proteins in H1975 cells and HCC827 cells after co-culture with vector B or MX1^{OE} B cells for 24 h. (**M**) Western blotting analysis of the indicated proteins in H1975 cells and HCC827 cells after culture with CM from vector B or MX1^{OE} B cells for 24 h

Based on the close relation between ISG$^+$ B cells and IFN-I, we next investigate whether ISG$^+$ B cells help promote the transformation of LUAD to SCLC through IFN-I, similar to ISG$^+$ T cells. Firstly, human CD19$^+$ B cells were infected with MX1^{OE} or vector lentivirus and incubated for 48 h to generate a stable MX1-overexpressing cell subline (MX1^{OE} B cells), mimicking ISG$^+$ B cells, and the corresponding control cell subline (Vector B cells) (Fig. 5K). Western blotting analyses further confirmed that MX1^{OE} lentivirus obviously upregulated MX1 expression at the protein level. Then H1975 and HCC827 cell lines were co-cultured with MX1^{OE} B cells or Vector B cells for 24 h. Co-culture significantly enhanced the expression of three neuroendocrine markers (Fig. 5L). Further treatment of both LUAD cell lines with medium conditioned by MX1^{OE} B cells similarly promoted the expression of neuroendocrine markers (Fig. 5M). Together, these findings indicated that IFN-I produced by MX1$^+$ B cells may contribute to the transdifferentiation from LUAD toward to a neuroendocrine cancer.

Identification of intercellular communication specially for epi 5 cells and ISG$^+$ lymphocytes and development of an ISG-associated signature

The tumor microenvironment is characterized by complex cell-cell interactions among different cell populations that ultimately modulate diverse biological processes, including SCLC transformation. Given that epi 5 was identified as a driving force of lineage plasticity, we focused on exploring intercellular communications specially involving epi 5 cells as senders or receivers (Fig. 6A, B and S6). Activated leukocyte cell adhesion molecule (ALCAM) signaling was significantly stronger when epi 5 cells interacted with ISG$^+$ T cells (Fig. 6C). To interrogate the information flow of ALCAM pathways more exactly, we further deployed ligand-receptor (L-R) pairs and found that the ALCAM-CD6 pair mediated this interaction (Fig. 6D). CD6, a T-cell costimulatory receptor, and its ligand ALCAM are involved in T cell activation and trafficking [38], suggesting that epi 5 cells may activate ISG$^+$ T cells through ALCAM-CD6 interaction. In addition, MK and FN1 signaling pathways were more activated between epi 5 and ISG$^+$ T cells compared with other T cell populations, as ITGA4 + ITGB1 receptors were more highly expressed in ISG$^+$ T cells (Fig. 6E and F, S7A and B). ITGA4 combines with ITGB1 on the cell surface to form the fully functional integrin very late antigen-4 (VLA-4), which helps inflammatory cells, particularly T lymphocytes, move toward to the given tissues [39]. Consequently, these findings suggest that ISG$^+$ T cells may migrate toward epi 5 cells via MK and FN1 signaling pathways.

Considering ISG$^+$ T cells and ISG$^+$ B cells mainly derived from T-SCLC patients, we next explored the interplay specifically between ISG$^+$ lymphocytes and other cell types. Despite the general similarities in the communication patterns between ISG$^+$ lymphocytes and other lymphocytes, GALECTIN signaling pathway was identified to be much more abundant in ISG$^+$ lymphocytes than other lymphocytes as an outgoing communication (Figure S7C). To further interrogate the ligand-receptor (L-R) pairs of GALECTIN pathways, we identified that LGALS9-CD45, LGALS9-CD44 and LGALS9-HAVCR2 were involved in the interaction of ISG$^+$ T cells and ISG$^+$ B with multiple cell types such as endothelial cells, B cells, T cells and myeloid cells (Figure S7D-F). Previous studies reported that galectin-9, encoded by *LGALS9*, interacts with PD-1 and mucin-domain containing-3 receptor (TIM-3) to regulate T cell death and immunotherapy efficacy. Thus, galectin-9 might be critical in regulating the immune response in T-SCLC and was a potential target for immunotherapy [40].

Given the crucial role of ISG$^+$ lymphocytes impact in shaping the TIME, particularly in pathological transformation, we next sought to identify key ISG-associated genes for predicting the OS of LUAD patients. Compared to other T and B cells, twenty-six ISG-related genes were significantly upregulated in both ISG$^+$ T and B cells (Fig. 6G). Among all the DEGs, we selected the top 65 genes to generate an ISG-associated signature, which was mainly expressed in immune cells but rarely observed in epithelial cells (Fig. 6H, Table S2). Then, multivariate Cox regression analyses were performed to calculate the regression coefficients for each gene of the signature. An activity scoring system was established based on a linear combination of gene expression levels, weighted by the regression coefficients, dividing patients into high-activity and low-activity groups. The prognostic performance of the activity scoring system based on ISG-associated signature was evaluated in a TCGA LUAD cohort, where the high-activity group had significantly worse

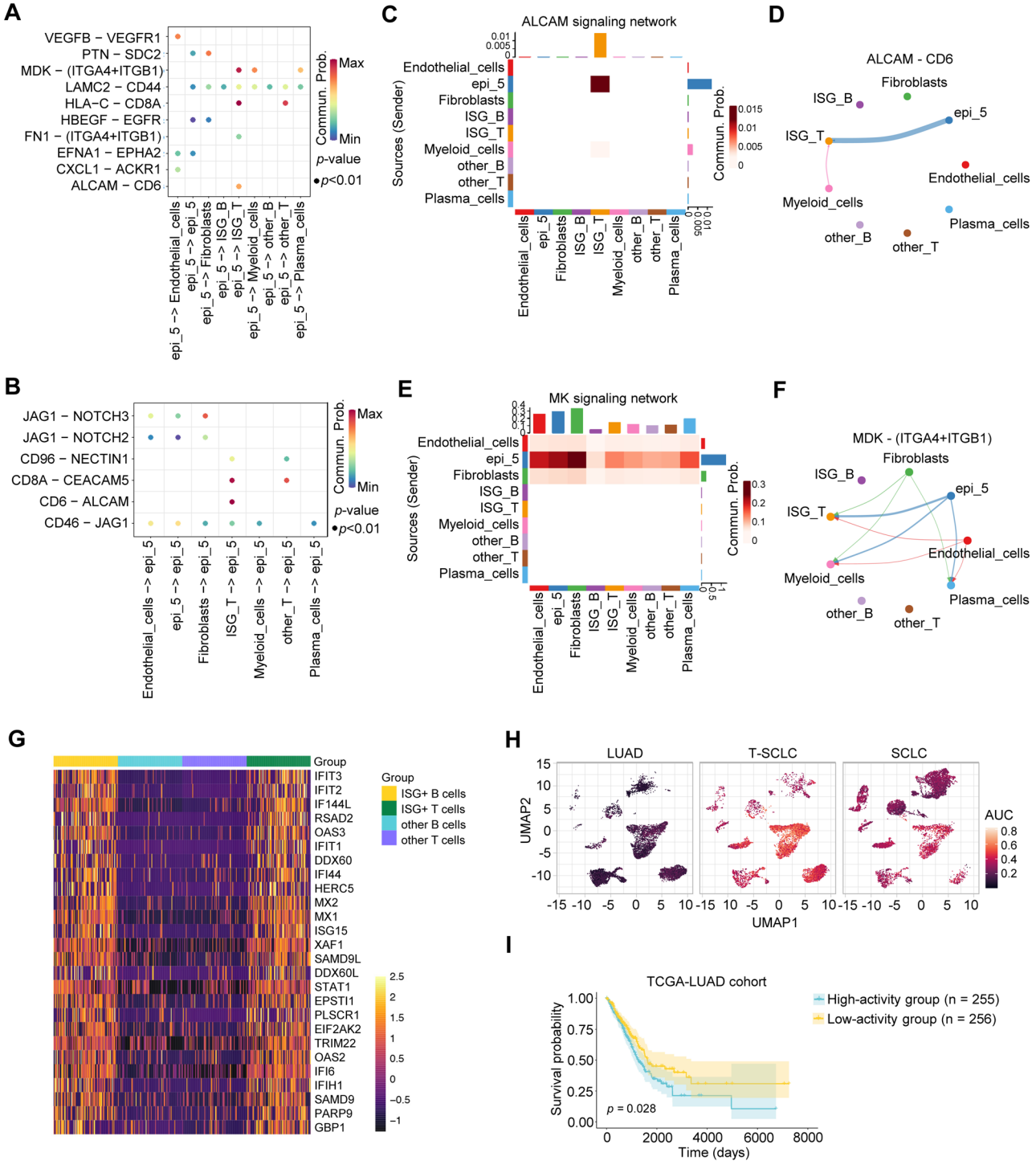

Fig. 6 Cell-cell interaction analysis targeting epithelial cluster 5 and ISG$^+$ T cells, and the development of ISG-associated gene signature. (**A**, **B**) Dot plots show selected outgoing and incoming communications of epi 5 cells through ligand-receptor pairs. (**C**) The Heatmap shows the activity of ALCAM signaling involved in the interactions between the 9 cell clusters. (**D**) The circle plot shows the predicted interactions mediated by ALCAM-CD6 in each pair of cell types. (**E**) The Heatmap shows the activity of MK signaling involved in the interactions between the 9 cell clusters. (**F**) The circle plot shows the predicted interactions mediated by MDK-(ITGA4 + ITGB1). (**G**) Heatmap of ISG-related significantly upregulated genes in ISG$^+$ B and T cells compared to other T and B cells. (**H**) UMAP plots of the expression of ISG-related signature in each cluster of the LUAD, T-SCLC and SCLC groups. (**I**) Kaplan-Meier survival curve for high-activity ($n = 255$) and low-activity ($n = 256$) groups in the TCGA-LUAD cohort. Survival curves were compared by the Log-Rank test ($p = 0.028$)

OS compared with the low-activity group ($p = 0.028$) (Fig. 6I). Given the above, the ISG-associated signature holds strong prognostic potential and may represent promising preventive and therapeutic targets for SCLC transformation.

Discussion

T-SCLC is defined as a distinct phenotype of SCLC, with a prognosis that is similar or even worse than the classic type of SCLC [8]. To date, the poor understanding of the transformation mechanism and the lack of effective treatments remain major obstacles to improve the survival of T-SCLC patients. Although increased attention has been paid to SCLC transformation in recent years, most studies have relied on rough bulk-sequencing due to the challenges of obtaining fresh sample. In the present study, we used scRNA-seq to provide the first high-resolution atlas of T-SCLC malignant cells and the surrounding immune microenvironment, comparing them with LUAD and *de novo* SCLC. We identified a stem-like malignant cell subpopulation with the potential for plasticity, as well as ISG^+ T and B clusters enriched in T-SCLC, potentially promoting SCLC transformation through IFN-I production. Moreover, we developed an ISG-associated signature and found that patients with high activity of this signature had poor OS.

Lineage plasticity, a fundamental property of cancer, enables tumor cells to shift between different cell states, has attracted increased interest in recent years. Currently intratumoral heterogeneity partly reflects the lineage plasticity of tumor cells. Here, we uncovered obviously more distinct clusters of tumor cells that co-existed in both T-SCLC and SCLC compared to LUAD. These clusters significantly differed in terms of marker genes, molecular signaling pathways, differentiation state and CNV profiles, indicating a dramatic increase in transcriptional heterogeneity during the process of SCLC transformation. Moreover, we verified the intermediate and transitional state of T-SCLC, as multiple genes and pathways showed consistent shifts from LUAD to T-SCLC and ultimately to SCLC, which has been reported previously based on bulk sequencing data [4, 41]. Notably, we detected an epithelial cluster shared among tumors across subtypes and groups, which demonstrated potent differentiation potential according to the transcriptional differentiation trajectory. Also, gene expression, pathway enrichment and mIF staining further point to the stem-like characteristic of this subpopulation, suggesting it as the potentially pioneering force of lineage plasticity for SCLC transformation. A more recent study using genetically engineered mouse models traced the histological transformation from LUAD to SCLC [30], identifying an undifferentiated, stem-like state emerges during the transformation, with the tumor cells exhibiting a "basal-like" appearance and activation of PI3K/AKT signaling pathway. Consistent with this, we found that epi 5 cells exhibited basal cell origins with marked upregulation of Notch and PI3K-AKT-mTOR signaling pathways. Moreover, the expression of the epi 5-associated gene module was gradually elevated along the histological transition in the mouse models. However, our analyses showed significant downregulation of MYC pathway in epi 5 cells, whereas *MYC* transcriptional output increased in a time-dependent manner along the transformation trajectory in the mouse model. This discordance may be partially attributed to the different subtypes of T-SCLC in our study, as MYC is known to promote a SCLC subtype temporal shift from ASCL1 to NEUROD1 to YAP1 [42]. At present cancer therapies mainly focus on a single oncogenic pathway or immune checkpoint but underestimate the high plasticity of tumor cells [43]. Targeting intratumoral heterogeneity or stem-like cells has been proposed as a novel strategy to overcome treatment resistance and disease progression [44, 45]. Therefore, further studies are warranted to elucidate the precise role of stem-like cells in SCLC transformation and to assess their potential therapeutic implications.

Further exploration of tumor-infiltrating immunocytes showed the immune microenvironment heterogeneity among the three groups, with different proportions of each cell cluster. More importantly, our data identified the enrichment of ISG^+ T cell and B cell subsets in T-SCLC for the first time, and mIF staining further validated this finding. Our study presented significant upregulation of IFN-I production and enrichment of IFN-I signaling in ISG^+ T and B cells, suggesting that these clusters are closely related to IFN-I. The role of IFN-I in tumor progression is highly complex, with activities that either suppress or promote tumor growth depending on the contexts. For instance, several studies have indicated that IFN-I mediates antineoplastic effects by modulating cancer immunoediting [46, 47]. Conversely, IFN-I has been reported to induce PD-L1 expression, thereby protecting cancer cells from T cell–mediated cytotoxicity [48, 49]. Notably, researchers have recently focused on the association between IFN and stemness. Muselle et al. have highlighted that IFN-I promotes the appearance of cancer stem cells with immune privilege and therapy resistance [50]. Moreover, IFN-γ produced by activated T cells even directly converts non-cancer stem cells to cancer stem cells, driving metastatic progression [51]. In this study, in vitro experiments revealed that IFN-Is promoted neuroendocrine differentiation in LUAD cells, but the cell morphology and growth rate did not show obviously changes, suggesting that IFN-Is may be important but insufficient to lead to SCLC transformation. Further research on molecular mechanisms would

broaden the understanding of the role of IFN-I in SCLC transformation.

Cell-to-cell communication, especially between the immune system and tumors, plays a pivotal role in tumor development and the response to treatments. The investigation of cell-cell interaction in T-SCLC revealed that epi 5 cells activated ISG$^+$ T cells via ALCAM signaling, while ISG$^+$ T cells migrated toward epi5 cells through VLA-4, an important receptor in the MK and FN1 signaling pathways. Previous multiple studies reported that VLA-4 played a critical role in T cell adhesion, trafficking, and transendothelial migration in response to "inside-out" signals initiated by chemokine and antigen receptors [52–55]. The results indicated close interaction between epi 5 cells and ISG$^+$ T cells, while no intercellular communication was observed with ISG$^+$ B cells. In addition, we disclosed that the GALECTIN pathway was specifically activated in ISG$^+$ T and B cells, facilitating crosstalk with myeloid cells, endothelial cells and also among themselves. Galectin-9 expression is induced by INF-I and reflects the IFN signature in systemic autoimmune disease [56]. Furthermore, as a well-established T cell inhibitory receptor, galectin-9 is known to mediate immunosuppression and is associated with poor prognosis in lung cancer [57]. Nowdays intercellular interaction has been widely recognized as the pharmacological basis of immunotherapy [58]. The most successful example to date is that of PD-1/PD-L1 immune checkpoint inhibitors. A previous study showed that disrupting the ALCAM-CD6 axis via ALCAM knockdown in non small cell lung cancer leads to increased inhibitory receptor scores on T cells and a significant reduction in activated T cells, potentially contributing to an immunosuppressive tumor microenvironment [59]. Another study by Morosi et al. demonstrated that suppression of ALCAM-CD6 communication impairs cDC1-CD8$^+$ T cell synapse formation [60]. In addition, a humanized IgG4 anti-VLA-4 monoclonal antibody effectively blocked transendothial and fibronectin-driven migration of CD4$^+$ and CD8$^+$ T cells [39]. On the contrary, both small-molecule activators and agonists of VLA-4, such as 7HP349 and THI0019, have been shown to facilitate the preferential localization of tumor-specific T cells to tumors [61, 62]. Consequently, disruptions in the interaction between epi 5 cells and ISG$^+$ T cells might hold great therapeutic potential for preventing or restraining SCLC transformation.

In recent years, the expansion of sample size and the diversity of data have increased the interest not only in exploring the key factors for tumor but also developing various models for prediction and prognosis [63, 64]. Considering the specific gene expression patterns of ISG$^+$ lymphocytes, we developed an ISG-associated gene signature that is significantly correlated with prognosis. Currently immunoproteomics, as an important bridge connecting the genome and phenotype, provides new strategies for generating more precisely predictive and prognostic models. Thus, it is worth further investigating the prognostic value of the ISG-associated gene signature in combination with proteomics in the future.

One limitation of the present study is the scarcity of T-SCLC samples due to the difficulty of obtaining fresh tissues, although we utilized the public mouse-model samples to further validate the findings. Therefore, a larger sample size study is warranted to establish the role of epi 5 and ISG$^+$ T cells in SCLC transformation. Nevertheless, our study provides a relatively complete picture of the TME in T-SCLC so far, laying the groundwork for further cellular and molecular explorations. In the future, as the advances of multi-omics and nanomaterials [12], the characteristics of epi 5 and ISG$^+$ T cells would offer valuable insights for guiding the development of therapeutic strategies, ultimately conquering this devastating disease.

Abbreviations

T-SCLC	Transformed small cell lung cancer
LUAD	Lung adenocarcinoma
NSCLC	Non-small cell lung cancer
mIF	Multiplex immunofluorescence
IFN-Is	Type I interferons
ISG$^+$	Interferon-stimulated gene-positive
CM	Conditioned medium
EGFR-TKIs	Epidermal growth factor receptor tyrosine kinase inhibitors
OS	Overall survival
GSEA	Gene set enrichment analysis
scRNA-seq	Single-cell RNA sequencing
CNV	Copy-number variation
AT2	Alveolar Type 2
DEGs	Differentially expressed genes
NK	Natural killer
KLR	Killer cell lectin-like receptors
ISP	Interferon stimulated protein
TIB	Tumor-infiltrating B cells and plasma cells
TFs	Transcription factors
STAT	signal transducer and activator of transcription
ISGF3	Interferon-stimulated gene factor 3
L-R	Ligand-receptor
TIM-3	T cell immunoglobulin and mucin-domain containing-3 receptor
PBS	Phosphate-buffered saline
ssGSVA	Single-sample Gene Set Variation Analysis

Supplementary Information

The online version contains supplementary material available at https://doi.org/10.1186/s12967-026-07940-6.

Supplementary Material 1: Document S1. Supplementary Figures S1-S7.

Supplementary Material 2: Table S1. Patient clinical and pathological characteristics. Related to Fig. 1.

Supplementary Material 3: Table S2. The list of sixty-five genes consisting the MX1 signature. Related to Fig. 6.

Supplementary Material 4: Table S3. Sequences for siRNA targeting IFNAR1 genes. Related to Methods.

Supplementary Material 5: Table S4. Primers for qRT-PCR. Related to Methods.

Supplementary Material 6

Acknowledgements
Not applicable.

Author contributions
J.H., Z.Z. and G.C. contributed equally to this work. J.H., J.J.Y. and J.W. conceived this project and designed the study. J.H., W.H. and J.J.Y. prepared patient tumor-tissue samples. J.H., Z.Z. and G.C. analyzed the data. J.H., Z.Z., G.C. and J.W. designed experiments design. J.H., Z.Z., G.C. and Y.Q.C. performed the experiments. J.Z., L.Y. and Q.Z. gave methodological support and conceptual advice. J.H., Z.Z., G.C., J.J.Y. and J.W. wrote the manuscript. All authors discussed the results and commented on the manuscript.

Funding
This research was supported by National Natural Science Foundation of China (82560596, 82373186), Shenzhen Medical Research Fund (C2501013), Guangdong Basic and Applied Basic Research Foundation (No. 2025A1515012700, No. 2022B1515130008), Guangzhou Science and Technology Bureau (No. 2025A04J4764), Jiangxi Province Natural Science Foundation (No. 20244BAB28024) and the Science and Technology Project in Ganzhou (2023LNS26799).

Data availability
The single-cell RNA-seq dataset and original code used to perform all analyses in this study are available in the GEO database as GSE319155. The public single-cell sequencing dataset applied in this study is available in the GEO database as GSE131907. Any additional information needed to reanalyze the data presented in this paper is available upon request from the corresponding author.

Declarations

Ethics approval and consent to participate
The study was approved by the Research Ethics Committee of Guangdong Provincial People's Hospital (No. GDREC2019304H(R1)) and was performed in accordance with the Declaration of Helsinki. All patients with T-SCLC and SCLC provided written informed consent for participation.

Consent for publication
All the authors agree to publication of the article.

Competing interests
The authors declare that they have no competing interests.

Author details
[1]Guangdong Lung Cancer Institute, Guangdong Provincial Key Laboratory of Translational Medicine in Lung Cancer, Guangdong Provincial People's Hospital, Guangdong Academy of Medical Sciences, Southern Medical University, Guangzhou 510080, China
[2]State Key Laboratory of Anti-Infective Drug Discovery and Development, School of Pharmaceutical Sciences, Sun Yat-sen University, Guangzhou 510006, China
[3]Department of Pathology, Guangdong Provincial People's Hospital, Guangdong Academy of Medical Sciences, Southern Medical University, Guangzhou 510080, China
[4]Department of Thoracic Surgery, The Third Affiliated Hospital, Sun Yat-sen University, Guangzhou, Guangdong 510630, China
[5]National-Local Joint Engineering Laboratory of Druggability and New Drugs Evaluation, Guangdong Provincial Key Laboratory of New Drug Design and Evaluation, Sun Yat-sen University, Guangzhou 510006, China
[6]Department of Oncology, Guangdong Provincial People's Hospital Ganzhou Hospital, Ganzhou 341000, China

Received: 29 October 2025 / Accepted: 21 February 2026
Published online: 04 March 2026

References

1. Clamon G, Zeitler W, An J, Hejleh TA. Transformational Changes Between Non-Small Cell and Small Cell Lung Cancer-Biological and Clinical Relevance-A Review. Am J Clin Oncol. 2020;43:670–5.
2. Offin M, Chan JM, Tenet M, Rizvi HA, Shen R, Riely GJ, Rekhtman N, Daneshbod Y, Quintanal-Villalonga A, Penson A, et al. Concurrent RB1 and TP53 Alterations Define a Subset of EGFR-Mutant Lung Cancers at risk for Histologic Transformation and Inferior Clinical Outcomes. J Thorac Oncol. 2019;14:1784–93.
3. Lee JK, Lee J, Kim S, Kim S, Youk J, Park S, An Y, Keam B, Kim DW, Heo DS, et al. Clonal History and Genetic Predictors of Transformation Into Small-Cell Carcinomas From Lung Adenocarcinomas. J Clin Oncol. 2017;35:3065–74.
4. Marcoux N, Gettinger SN, O'Kane G, Arbour KC, Neal JW, Husain H, Evans TL, Brahmer JR, Muzikansky A, Bonomi PD, et al. EGFR-Mutant Adenocarcinomas That Transform to Small-Cell Lung Cancer and Other Neuroendocrine Carcinomas: Clinical Outcomes. J Clin Oncol. 2019;37:278–85.
5. Wang W, Xu C, Chen H, Jia J, Wang L, Feng H, Wang H, Song Z, Yang N, Zhang Y. Genomic alterations and clinical outcomes in patients with lung adenocarcinoma with transformation to small cell lung cancer after treatment with EGFR tyrosine kinase inhibitors: A multicenter retrospective study. Lung Cancer. 2021;155:20–7.
6. Quintanal-Villalonga A, Taniguchi H, Zhan YA, Hasan MM, Chavan SS, Meng F, Uddin F, Manoj P, Donoghue MTA, Won HH, et al. Multiomic Analysis of Lung Tumors Defines Pathways Activated in Neuroendocrine Transformation. Cancer Discov. 2021;11:3028–47.
7. Huang J, Zhang SL, Zhang C, Huang W, Zhang Z, Chen YQ, Su JW, Yan HH, Chen HJ, Yang JJ, et al. Genotyping of RB1 status identifies two distinct subtypes in EGFR-mutant lung cancers with SCLC transformation. Clin Transl Med. 2024;14:e1683.
8. Quintanal-Villalonga A, Chan JM, Yu HA, Pe'er D, Sawyers CL, Sen T, Rudin CM. Lineage plasticity in cancer: a shared pathway of therapeutic resistance. Nat Rev Clin Oncol. 2020;17:360–71.
9. Cozar B, Greppi M, Carpentier S, Narni-Mancinelli E, Chiossone L, Vivier E. Tumor-Infiltrating Natural Killer Cells. Cancer Discov. 2021;11:34–44.
10. Kim N, Kim HK, Lee K, Hong Y, Cho JH, Choi JW, Lee JI, Suh YL, Ku BM, Eum HH, et al. Single-cell RNA sequencing demonstrates the molecular and cellular reprogramming of metastatic lung adenocarcinoma. Nat Commun. 2020;11:2285.
11. Yang L, He YT, Dong S, Wei XW, Chen ZH, Zhang B, Chen WD, Yang XR, Wang F, Shang XM, et al. Single-cell transcriptome analysis revealed a suppressive tumor immune microenvironment in EGFR mutant lung adenocarcinoma. J Immunother Cancer. 2022;10.
12. Chen L, Lin A, Tang B, Li K, Qian Y, Liu X, Zhang Y, Deng Y, Chen W, Zhao Q, Miao K. The Future of Cancer Therapy: Nanomaterials and Tumor Microenvironment. iMetaMed. 2025;1:e70007.
13. Korsunsky I, Millard N, Fan J, Slowikowski K, Zhang F, Wei K, Baglaenko Y, Brenner M, Loh PR, Raychaudhuri S. Fast, sensitive and accurate integration of single-cell data with Harmony. Nat Methods. 2019;16:1289–96.
14. Zhao J, Jaffe A, Li H, Lindenbaum O, Sefik E, Jackson R, Cheng X, Flavell RA, Kluger Y. Detection of differentially abundant cell subpopulations in scRNA-seq data. Proc Natl Acad Sci USA. 2021;118.
15. Cao J, Spielmann M, Qiu X, Huang X, Ibrahim DM, Hill AJ, Zhang F, Mundlos S, Christiansen L, Steemers FJ, et al. The single-cell transcriptional landscape of mammalian organogenesis. Nature. 2019;566:496–502.
16. Hanzelmann S, Castelo R, Guinney J. GSVA: gene set variation analysis for microarray and RNA-seq data. BMC Bioinformatics. 2013;14:7.
17. Andreatta M, Carmona SJ, UCell. Robust and scalable single-cell gene signature scoring. Comput Struct Biotechnol J. 2021;19:3796–8.
18. Wang J, Zou JX, Xue X, Cai D, Zhang Y, Duan Z, Xiang Q, Yang JC, Louie MC, Borowsky AD, et al. ROR-gamma drives androgen receptor expression and represents a therapeutic target in castration-resistant prostate cancer. Nat Med. 2016;22:488–96.
19. Cai D, Wang J, Gao B, Li J, Wu F, Zou JX, Xu J, Jiang Y, Zou H, Huang Z, et al. RORgamma is a targetable master regulator of cholesterol biosynthesis in a cancer subtype. Nat Commun. 2019;10:4621.
20. Van den Berge K, de Bezieux R, Street H, Saelens K, Cannoodt W, Saeys R, Dudoit Y, S., and, Clement L. Trajectory-based differential expression analysis for single-cell sequencing data. Nat Commun. 2020;11:1201.
21. Jin S, Guerrero-Juarez CF, Zhang L, Chang I, Ramos R, Kuan CH, Myung P, Plikus MV, Nie Q. Inference and analysis of cell-cell communication using CellChat. Nat Commun. 2021;12:1088.
22. Stewart CA, Gay CM, Xi Y, Sivajothi S, Sivakamasundari V, Fujimoto J, Bolisetty M, Hartsfield PM, Balasubramaniyan V, Chalishazar MD, et al. Single-cell analyses reveal increased intratumoral heterogeneity after the onset of therapy resistance in small-cell lung cancer. Nat Cancer. 2020;1:423–36.

23. Tian Y, Li Q, Yang Z, Zhang S, Xu J, Wang Z, Bai H, Duan J, Zheng B, Li W, et al. Single-cell transcriptomic profiling reveals the tumor heterogeneity of small-cell lung cancer. Signal Transduct Target Ther. 2022;7:346.
24. Chan JM, Quintanal-Villalonga A, Gao VR, Xie Y, Allaj V, Chaudhary O, Masilionis I, Egger J, Chow A, Walle T, et al. Signatures of plasticity, metastasis, and immunosuppression in an atlas of human small cell lung cancer. Cancer Cell. 2021;39:1479–96. e1418.
25. Neptune ER, Podowski M, Calvi C, Cho JH, Garcia JG, Tuder R, Linnoila RI, Tsai MJ, Dietz HC. Targeted disruption of NeuroD, a proneural basic helix-loop-helix factor, impairs distal lung formation and neuroendocrine morphology in the neonatal lung. J Biol Chem. 2008;283:21160–9.
26. Borges M, Linnoila RI, van de Velde HJ, Chen H, Nelkin BD, Mabry M, Baylin SB, Ball DW. An achaete-scute homologue essential for neuroendocrine differentiation in the lung. Nature. 1997;386:852–5.
27. Sarode P, Mansouri S, Karger A, Schaefer MB, Grimminger F, Seeger W, Savai R. Epithelial cell plasticity defines heterogeneity in lung cancer. Cell Signal. 2020;65:109463.
28. Cheung WK, Nguyen DX. Lineage factors and differentiation states in lung cancer progression. Oncogene. 2015;34:5771–80.
29. Rudin CM, Poirier JT, Byers LA, Dive C, Dowlati A, George J, Heymach JV, Johnson JE, Lehman JM, MacPherson D, et al. Molecular subtypes of small cell lung cancer: a synthesis of human and mouse model data. Nat Rev Cancer. 2019;19:289–97.
30. Gardner EE, Earlie EM, Li K, Thomas J, Hubisz MJ, Stein BD, Zhang C, Cantley LC, Laughney AM, Varmus H. Lineage-specific intolerance to oncogenic drivers restricts histological transformation. Science. 2024;383:eadj1415.
31. Moreira S, Polena E, Gordon V, Abdulla S, Mahendram S, Cao J, Blais A, Wood GA, Dvorkin-Gheva A, Doble BW. A Single TCF Transcription Factor, Regardless of Its Activation Capacity, Is Sufficient for Effective Trilineage Differentiation of ESCs. Cell Rep. 2017;20:2424–38.
32. Christin JR, Wang C, Chung CY, Liu Y, Dravis C, Tang W, Oktay MH, Wahl GM, Guo W. Stem Cell Determinant SOX9 Promotes Lineage Plasticity and Progression in Basal-like Breast Cancer. Cell Rep. 2020;31:107742.
33. Lin A, Ye P, Li Z, Jiang A, Liu Z, Cheng Q, Zhang J, Luo P. Natural killer cell immune checkpoints and their therapeutic targeting in cancer treatment. Research (Wash D C). 2025;8:0723.
34. Huang J, Zhang SL, Zhou C, Huang W, Luo P, Chen HJ, Yang JJ. Genomic and Transcriptomic Analysis of Neuroendocrine Transformation in ALK-Rearranged Lung Adenocarcinoma After Treatments With Sequential ALK Inhibitors: A Brief Report. JTO Clin Res Rep. 2022;3:100338.
35. Morgan D, Tergaonkar V. Unraveling B cell trajectories at single cell resolution. Trends Immunol. 2022;43:210–29.
36. Jefferies CA. Regulating IRFs in IFN Driven Disease. Front Immunol. 2019;10:325.
37. Philips RL, Wang Y, Cheon H, Kanno Y, Gadina M, Sartorelli V, Horvath CM, Darnell JE Jr., Stark GR, O'Shea JJ. The JAK-STAT pathway at 30: Much learned, much more to do. Cell. 2022;185:3857–76.
38. Rambaldi B, Kim HT, Arihara Y, Asano T, Reynolds C, Manter M, Halpern M, Weber A, Koreth J, Cutler C, et al. Phenotypic and functional characterization of the CD6-ALCAM T-cell co-stimulatory pathway after allogeneic cell transplantation. Haematologica. 2022;107:2617–29.
39. Savino W, Chaves B, Bonomo AC, Cotta-de-Almeida V. Integrin-directed antibody-based immunotherapy: focus on VLA-4. Immunother Adv. 2021;1:ltab002.
40. Yang R, Sun L, Li CF, Wang YH, Yao J, Li H, Yan M, Chang WC, Hsu JM, Cha JH, et al. Galectin-9 interacts with PD-1 and TIM-3 to regulate T cell death and is a target for cancer immunotherapy. Nat Commun. 2021;12:832.
41. Foster NR, Qi Y, Shi Q, Krook JE, Kugler JW, Jett JR, Molina JR, Schild SE, Adjei AA, Mandrekar SJ. Tumor response and progression-free survival as potential surrogate endpoints for overall survival in extensive stage small-cell lung cancer: findings on the basis of North Central Cancer Treatment Group trials. Cancer. 2011;117:1262–71.
42. Ireland AS, Micinski AM, Kastner DW, Guo B, Wait SJ, Spainhower KB, Conley CC, Chen OS, Guthrie MR, Soltero D, et al. MYC Drives Temporal Evolution of Small Cell Lung Cancer Subtypes by Reprogramming Neuroendocrine Fate. Cancer Cell. 2020;38:60–78. e12.
43. Deng X, Ma N, He J, Xu F, Zou G. The Role of TGFBR3 in the Development of Lung Cancer. Protein Pept Lett. 2024;31:491–503.
44. Zhang XF, Zuo XY, Zhu Y, Li JX, Xian JS, Zhang WX, Cheng W, Yuan J, Gong YF, Tang H, et al. Targeting cell-state plasticity driven by FOXM1/CEBPB axis disrupts developmental heterogeneity and therapeutic resistance in hepatocellular carcinoma. J Hepatol. 2025.
45. Li MM, He YT, Liang JK, Guan XY, Ma NF, Liu M. Cancer stem cell-mediated therapeutic resistance in hepatocellular carcinoma. Hepatoma Res. 2022;8.
46. Moschos S, Varanasi S, Kirkwood JM. Interferons in the treatment of solid tumors. Cancer Treat Res. 2005;126:207–41.
47. Zitvogel L, Galluzzi L, Kepp O, Smyth MJ, Kroemer G. Type I interferons in anticancer immunity. Nat Rev Immunol. 2015;15:405–14.
48. Garcia-Diaz A, Shin DS, Moreno BH, Saco J, Escuin-Ordinas H, Rodriguez GA, Zaretsky JM, Sun L, Hugo W, Wang X, et al. Interferon Receptor Signaling Pathways Regulating PD-L1 and PD-L2 Expression. Cell Rep. 2017;19:1189–201.
49. Chen J, Cao Y, Markelc B, Kaeppler J, Vermeer JA, Muschel RJ. Type I IFN protects cancer cells from CD8 + T cell-mediated cytotoxicity after radiation. J Clin Invest. 2019;129:4224–38.
50. Musella M, Guarracino A, Manduca N, Galassi C, Ruggiero E, Potenza A, Maccafeo E, Manic G, Mattiello L, Rehim SA. Type I IFNs promote cancer cell stemness by triggering the epigenetic regulator KDM1B. Nat Immunol. 2022;23:1379–92.
51. Beziaud L, Young CM, Alonso AM, Norkin M, Minafra AR, Huelsken J. IFNgamma-induced stem-like state of cancer cells as a driver of metastatic progression following immunotherapy. Cell Stem Cell. 2023;30:818–31. e816.
52. Sixt M, Bauer M, Lammermann T, Fassler R. Beta1 integrins: zip codes and signaling relay for blood cells. Curr Opin Cell Biol. 2006;18:482–90.
53. Sato T, Tachibana K, Nojima Y, D'Avirro N, Morimoto C. Role of the VLA-4 molecule in T cell costimulation. Identification of the tyrosine phosphorylation pattern induced by the ligation of VLA-4. J Immunol. 1995;155:2938–47.
54. Davis LS, Oppenheimer-Marks N, Bednarczyk JL, McIntyre BW, Lipsky PE. Fibronectin promotes proliferation of naive and memory T cells by signaling through both the VLA-4 and VLA-5 integrin molecules. J Immunol. 1990;145:785–93.
55. Mittelbrunn M, Molina A, Escribese MM, Yanez-Mo M, Escudero E, Ursa A, Tejedor R, Mampaso F, Sanchez-Madrid F. VLA-4 integrin concentrates at the peripheral supramolecular activation complex of the immune synapse and drives T helper 1 responses. Proc Natl Acad Sci U S A. 2004;101:11058–63.
56. van den Hoogen LL, van der Heijden EHM, Hillen MR, Mertens JS, Fritsch-Stork RDE, Radstake T, van Roon JAG. Galectin-9 reflects the interferon signature and correlates with disease activity in systemic autoimmune diseases. Response to: 'Biomarkers: to be or not to be' by Yavuz and Ronnblom. Ann Rheum Dis. 2020;79:e9.
57. He Y, Jia K, Dziadziuszko R, Zhao S, Zhang X, Deng J, Wang H, Hirsch FR, Zhou C. Galectin-9 in non-small cell lung cancer. Lung Cancer. 2019;136:80–5.
58. Maffuid K, Cao Y. Decoding the complexity of immune-cancer cell interactions: empowering the future of cancer immunotherapy. Cancers (Basel). 2023;15.
59. Wen S, Du X, Zhu M, Huang C, Lin Z, Li M, Hu B, Wang X, Jiang F, Zhou G, et al. ALCAM-CD6 axis suppression: a key determinant of immune-mediated metastasis recurrence in stage III non-small cell lung cancer. J Immunother Cancer. 2025;13.
60. Morosi LG, Piperno GM, Lopez L, Amadio R, Joshi S, Rustighi A, Del Sal G, Benvenuti F. ALCAM-mediated cDC1 CD8 T cells interactions are suppressed in advanced lung tumors. Oncoimmunology. 2024;13:2367843.
61. Hickman A, Koetsier J, Kurtanich T, Nielsen MC, Winn G, Wang Y, Bentebibel SE, Shi L, Punt S, Williams L, et al. LFA-1 activation enriches tumor-specific T cells in a cold tumor model and synergizes with CTLA-4 blockade. J Clin Invest. 2022;132.
62. Vanderslice P, Biediger RJ, Woodside DG, Brown WS, Khounlo S, Warier ND, Gundlach CWT, Caivano AR, Bornmann WG, Maxwell DS, et al. Small molecule agonist of very late antigen-4 (VLA-4) integrin induces progenitor cell adhesion. J Biol Chem. 2013;288:19414–19428.
63. Yang L, Li S, Bai G, Li L, Li Y, Liang X, Ye Z, Li L, Zhuang L, Guan J, Gong W. Immunometabolic Features and Key Biomarkers in Lung Cancer Complicated by Pulmonary Tuberculosis: Insights From Transcriptome and Clinical. Cohort Anal. 2025;1:e70015.
64. Liu L, Xie Y, Yang H, Lin A, Dong M, Wang H, Zhang C, Liu Z, Cheng Q, Zhang J, et al. HPVTIMER: A shiny web application for tumor immune estimation in human papillomavirus-associated cancers. Imeta. 2023;2:e130.

Publisher's note